

Article

Sizing of Battery Energy Storage Systems for Firming PV Power including Aging Analysis

Juan A. Tejero-Gómez  and Ángel A. Bayod-Rújula * 

Department of Electrical Engineering, University of Zaragoza, 50018 Zaragoza, Spain; jatejero@unizar.es

* Correspondence: aabayod@unizar.es

Abstract: The variability of solar radiation presents significant challenges for the integration of solar photovoltaic (PV) energy into the electrical system. Incorporating battery storage technologies ensures energy reliability and promotes sustainable growth. In this work, an energy analysis is carried out to determine the installation size and the operating setpoint with optimal constant monthly power through an iterative calculation process, considering various operating setpoints and system parameters. A degradation model is integrated according to the curves offered by battery manufacturers and the charge–discharge cycles are calculated using the rainflow method to guarantee a reliable analysis of the plant. Through massive data analysis in a long-term simulation, indicators are generated that allow for establishing a relationship between the energy unavailability of the system and the BESS dimensions.

Keywords: large-scale battery energy storage system; utility-scale PV-plus-battery; aging; battery degradation; firm power

1. Introduction

The global energy system is currently undergoing a transition towards a new paradigm characterized by decarbonization, the decentralization of generation, the electrification of the economy and a more sustainable use of resources. Thanks to technological advances and cost reduction, the implementation of electrical energy production systems is increasingly high. They represent a high percentage of the total power of the generation system and contribute to an increasing extent to the production mix of electric power. The increase in renewables as a share of energy supply in 2022 was the second largest in history. A total of 25% of the electricity generated worldwide was the responsibility of renewable photovoltaic and wind generation plants [1]. Even faster increases are needed to align with the Net Zero Emissions Scenario [2]. The European Green Deal establishes the pace of decarbonization required in the coming years [3].

Electrical generation from renewable energies is associated with the resources (wind, photovoltaic) and is variable, intermittent and not dispatchable. Whilst the penetration of these generation sources is not high, they do not pose major problems for the operation and security of the electrical networks to which they are connected. But the high implementation of renewable energy is a challenge [4]. High voltage variations and fluctuations or strong ramps may occur in the generation curves. This requires greater power capacity available in the electrical network and requires other flexible systems, both for generation and the response to demand.

In the planning process for new plants, power companies set limitations on the amount of power that can be connected. Relevant limitations are usually placed on the maximum power that can be injected into the network to limit these voltage fluctuations. The studies are usually conducted based on considering the most unfavorable situation for the system, that is, moments of very high production (the nominal power of the inverters is usually considered). However, such a high generation is produced in very few hours a year. This



Citation: Tejero-Gómez, J.A.; Bayod-Rújula, Á.A. Sizing of Battery Energy Storage Systems for Firming PV Power including Aging Analysis. *Energies* **2024**, *17*, 1485. <https://doi.org/10.3390/en17061485>

Academic Editor: Abdul-Ghani Olabi

Received: 23 February 2024

Revised: 13 March 2024

Accepted: 17 March 2024

Published: 20 March 2024



Copyright: © 2024 by the authors. Licensee MDPI, Basel, Switzerland. This article is an open access article distributed under the terms and conditions of the Creative Commons Attribution (CC BY) license (<https://creativecommons.org/licenses/by/4.0/>).

hinders the further implementation of photovoltaic plants, or the need to reinforce lines and substations. The operation of the electric companies' assets is therefore very restricted since their capacity to conduct electrical energy is limited by the maximum values, and most of the time they are thus underused. But the maximum power is produced in very few moments a year, so the capacity of the networks is underutilized.

Owners of photovoltaic installations are also affected due to these characteristics of their systems. With the progressive increase in photovoltaic production during the central hours of the day, MWh prices tend to be very low precisely at the times of greatest production. This effect called "cannibalization" represents a reduction in its benefits, so its economic viability is compromised. At times when there is excess generation, curtailments are necessary, which further reduce its economic viability. These curtailments are becoming higher in some countries. On the other hand, energy generation from photovoltaic plants is subject to forecasting errors, which incur penalizing costs [5].

Accuracy in long-term estimates of energy production, with time horizons greater than one year, is of utmost importance for the technical planning of future distributed generation (DG) units. An adequate estimate allows for the correct allocation of resources, the optimization of the infrastructure and the better integration of the DG units into the energy system. As baseload generation from the combustion of fossil fuels is replaced by renewable energy sources; ensuring reliable capacity firming support for the power grid will become crucial. Firm energy determines the maximum volume of energy that a generation unit can sell with a given level of reliability. The capacity value (or "capacity credit") indicates the extent to which ERVs can be relied upon just like conventional power plants. The capacity value of solar photovoltaic (PV) is very low [6–8].

The definition of the appropriate mechanisms to achieve the complete integration of renewable energies into the energy system is still under development. The selection of these mechanisms will depend on a variety of factors, including the climatic conditions of the area, policies implemented by the government, the specific geographical location and changes in costs that are revealed through techno-economic analyses [9].

In this context, storage systems are positioned as a necessary technology to allow for the adequate grid integration of the growing renewable power. In order to move towards the net zero scenario, storage capacity must be significantly increased, reaching an annual average of 80 GW during the period between 2022 and 2030 [6], and it is necessary to exploit different options. In particular, battery energy storage systems (BESSs) can offer such robust capacity, giving the system management capabilities for the generated PV energy. The storage industry is projected to grow to hundreds of times its current size in the coming decades. The dataset [10] points to a considerable reduction in the prices of lithium-ion storage systems in utility applications over the last decade. The average cost has decreased from \$1659/kWh in 2010 to \$285/kWh in 2021.

Security of supply is a key factor in the electrical system. Installing batteries in parallel reduces overgeneration and the cutting and sale of energy during peak production hours. BESSs can offer firm capacity, providing the system with management capabilities for the generated photovoltaic energy. However, for economic reasons, it has been rare until now to discuss the operation of large-scale PV plants operating as baseload generation plants. From the point of view of hosting capacity, the power to be taken into account for the PV-BESS would no longer be the peak power of the collector field, but rather the constant power to be delivered to the network. This increases the number of facilities that fit into a given distribution network [11]. For example, in Spain, the total nominal power of the distributed generators (DGs) should be less than 50% of the nominal capacity of the Medium Voltage/Low Voltage (MV/LV) transformer at the interconnection point [12].

Another benefit of capacity firming is that the system and all its components operate close to their nominal power ratings for a longer time. Furthermore, the cost of converters in large-scale PV plants will be lower due to the power output smoothing that is supplied to the grid.

Unlike conventional substations, a substation for a large-scale PV plant has an uneven utilization coefficient due to the characteristics of solar radiation. BESSs can shift the peak of daytime photovoltaic production to the night. Furthermore, the capacity of the transformer of the substation connected to the photovoltaic plant can be decreased by directing the generation peaks of the solar panels towards the BESS [9] for subsequent supply.

Due to all of the above, the concept of constant photovoltaic power generation (PV-CPG) arises to overcome these problems. The problems of voltage variations due to variable currents, ramps, the need for backup sources, the cannibalization effect, etc., are reduced.

References [13–16] accurately determine the optimal capacity of battery energy storage systems (BESSs) when integrated with renewable energy sources, taking into account the effects of battery degradation. Although the main thrust of these studies bears some resemblance to the present manuscript, they are not directly comparable. They focus on economic analysis. Our manuscript aims to completely abstract from economic analysis and focus exclusively on energy aspects. Furthermore, this model lacks comparability in terms of degradation, since the system does not provide a 24 h baseload.

In [14], iterative methods are used, similar to the approach presented in this manuscript. However, it is important to note that the proposed degradation model is rather simplified and is based solely on another author's model.

Study [15] is consistent with our manuscript but focuses specifically on extremely fast charging stations.

The proposed system is designed to provide firm power or backup capacity to the electricity system. This steady flow of power from the generating plant is guaranteed with a high level of reliability. Therefore, its massive integration into the power grid could lead to a reduction in the need for frequency regulation technologies, as a high level of available power is guaranteed with reduced uncertainty. Some examples of firming power in the literature are the following.

In [8], the goal is to achieve constant power output from 24 h to a few hours during the day. In [17], a battery management and control algorithm mitigates fluctuations in intermittent PV generation for hourly periods. In [18], the required energy storage capacity is estimated in order to guarantee the constant and reliable delivery of energy by wind and photovoltaic means in Japan's electrical system.

A 50 MW AC PV system with 60 MW/240 MWh battery storage modeled in California can provide >98% capacity factor over a 7–10 p.m. target period with a lower lifetime cost of operation than a conventional combustion turbine natural gas power plant [19]. However, this scenario is conservative, and it is not proposed to establish a 24 h baseload as proposed in the present study. In a similar way, in [20], the storage is dimensioned for a large PV plant with storage in baseload operation.

In [5], PV production is regulated with BESSs to maintain a constant output level, which significantly contributes to power grid stability, but only in a certain time interval during the day. In [21], an analysis of the optimal relationship between the optimal size of the required battery and the peak power of the generation system is presented, as well as the optimal operating setpoint of a PV + STG system to provide firm capacity all year.

Given that the solar resource is notably lower in the winter months, a similar analysis was presented in [22] but for constant operating setpoints on a monthly basis.

All these cases mentioned are conservative and do not propose to establish a 24 h baseload. They also do not take into account degradation phenomena in the BESS, as proposed in this study.

The present study is conceived within the framework of a planning phase for the electric grid and focuses on the technical optimization between a PV plant and the BESS, where the main requirement is the supply of a 24 h baseload generation of the system, defined as the production of constant and continuous energy 24 h a day. This means that the generation does not fluctuate and remains stable at all times, meeting the definition of baseload generation. In addition, a proven battery degradation model is integrated, and

charge–discharge cycles are accurately calculated using the rainflow-counting algorithm to ensure reliable plant analysis.

The proposed study identifies the optimal dimensions of a PV plant hybridized with a battery energy storage system that supplies a constant power setpoint during monthly intervals. Through massive data analysis in a long-term simulation, indicators are generated that establish a relationship between the energy unavailability of the system and the BESS dimensions. Through an iterative calculation process, considering various operating instructions and system parameters, a comparative analysis is carried out with the purpose of determining the optimal installation size for each scenario.

The aging effects of lithium-ion battery storage systems have been considered, according to the curves offered by battery manufacturers. The replacement of the battery bank at the end of its useful life has also been taken into account.

This manuscript proposes an innovative and risky study that may not be economically feasible at this time. It therefore focuses on calculating energy balances and is conceived within the framework of a planning phase for the electric grid and focuses on the technical optimization between a PV plant and the BESS, where the main requirement is the supply of a 24 h baseload generation of the system, defined as the production of constant and continuous energy 24 h a day.

The remainder of this paper is organized as follows: Section 2 presents the proposed model detailing its equations, phases, parameters and indicators. In addition, the modeling of the BESS degradation is included. The results of the simulation are shown in Section 3. In Section 4, conclusions are drawn.

2. Case Study

2.1. Problem Formulation

The aim is to transform a photovoltaic production profile, which has a characteristic bell-shaped shape, into a continuous and constant supply of power that remains uniform throughout 24 h a day with high guarantees of availability. A typical daily profile comparing both curves is shown in Figure 1.

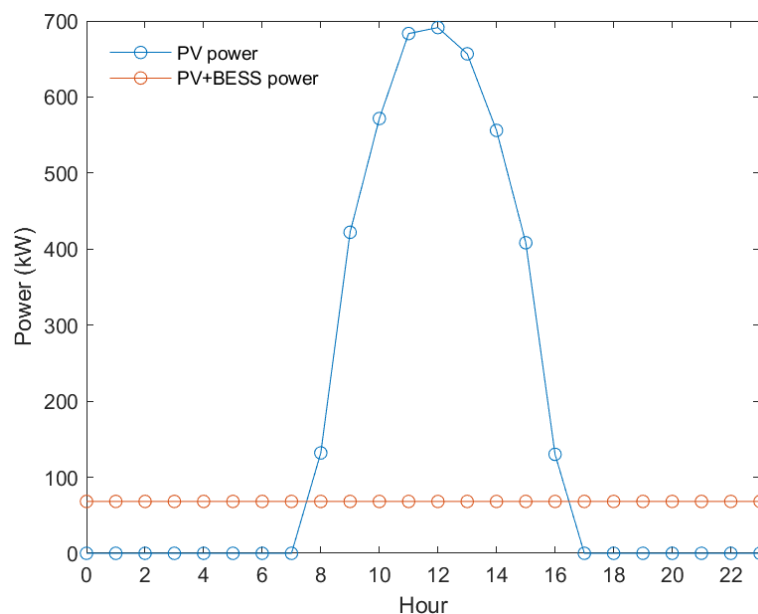


Figure 1. A typical profile for PV-BESS energy for a typical winter day (3 January).

2.2. Proposed Model

In coherence with our previous research [21,22], the present study continues with the analysis of the behavior of a PV-BESS hybrid plant. The quantification of the BESS degradation and the appropriate assignment of the constant power are carried out for a

correct evaluation of the system. The temporal frequency and the geographical point are fundamental components when defining the methodology of the study. Time frequency refers to the regularity with which data are collected and analyzed over time. The evaluation of large-scale PV plants, integrated into the electrical grid, can be achieved effectively through the use of hourly data [23]. The short-term variability inherent to photovoltaic generation is mitigated by the periodicity of solar radiation over a broader set of time. The Sun exhibits cyclical patterns with a periodicity of around 11 years. For this reason, it is proposed to carry out a simulation that covers a period of 11 years starting from 2006. On the other hand, the geographical point refers to the specific location where the data are collected. In the present case, the School of Engineering and Architecture of the University of Zaragoza, located on María de Luna Street in Zaragoza, Spain, has been selected as the geographical point of reference. Since plant PV production is linked to the amount of solar irradiation, selecting a specific site involves collecting data for representative conditions unique to that region. However, it is possible to extrapolate the results to any region by modifying the irradiance data. Therefore, although the study is carried out in a specific location, its findings may have much broader relevance and applicability.

A simplified scheme of the proposed PV-BESS system is illustrated in Figure 2. The photovoltaic plant transfers the generated energy to the electrical system through the inverter group. For its part, the energy storage system (BESS) has the capacity to inject energy into the system at times when the photovoltaic plant cannot satisfy the demand or, alternatively, to store the surplus energy generated by the photovoltaic system. It is imperative that, at the point of common coupling (PCC), a constant power setpoint is maintained to guarantee the reliability of the system.

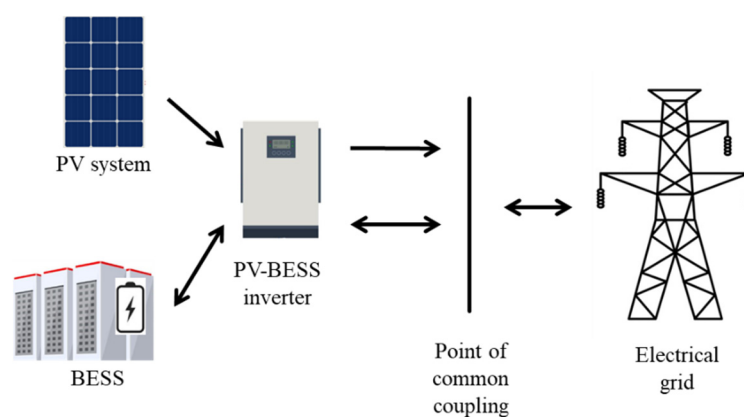


Figure 2. Scheme of the PV-BESS system.

By analyzing extensive photovoltaic production datasets, there is a tendency to neutralize fluctuations over short time horizons due to incidents or cloud cover. The algorithm developed in MATLAB R2021a classifies photovoltaic production according to months, thus identifying inherent seasonal patterns. In this way, the system power setpoint is adjusted monthly, based on the estimated photovoltaic production.

The efficiency of a PV-BESS is influenced by the power ratio between both components. Since the charging operation of the BESS is limited to the power generated by the PV plant, any power of the BESS that exceeds the power of the photovoltaic generation may be inefficient. Therefore, to avoid the underutilization of the BESS, a restriction is established that the power of the BESS must be less than the peak power of the photovoltaic generation ($P_{\text{BESS}} = 1 \text{ MW}$).

In the context of a preliminary theoretical analysis, the sizing of the BESS is addressed under a hypothesis of a daily balance between energy production and its supply. According to this model, the BESS is charged during peak daytime generation hours and discharged during the remaining hours to ensure the supply of a constant baseload. For the specific case of the location of this study, according to the PVGIS website [24], it is determined that

the average daily production of a PV plant is 4.36 kWh/kW. Therefore, for a 1 MW PV plant, the theoretical capacity of the BESS required to displace energy production at any time of the day would be up to 4.36 MWh. Therefore, the approximate C-rate of the BESS is 0.23.

2.3. Model Equations

In this paper, part of the model previously proposed in [21,22] is used. Following that, the equations that characterize the PV-BESS model are briefly described.

For the PV plant, 2041 Tallmax TSM-DE15V(II) 490W monocrystalline photovoltaic modules are selected, developed in China by Trinasolar for utility-scale PV applications [25].

Using Equations (1)–(3), the photovoltaic production for each hour is obtained. PV output was simulated for fixed systems facing south at 35° tilt.

For an accurate assessment of PV production in a specific area, it is crucial to have long periods of irradiance data. This is because solar irradiance is subject to significant variations resulting from changes in meteorological and seasonal conditions. The long-term solar radiation data are analyzed for a period of 11 years, taking the hourly irradiance from the PVGIS database [24]. The temperature reached by the PV cells is defined in Equation (1) when the module is exposed to operating conditions. This temperature is influenced by the ambient temperature and irradiance.

$$T_C = T_A + G_M \cdot \frac{\text{NOCT} - 20}{800} \quad (1)$$

where

- T_C is the module temperature [°C].
- T_A is the ambient temperature [°C].
- G_M is the global irradiance incident [$\text{W} \cdot \text{m}^{-2}$].
- NOCT is the Nominal Operating Cell Temperature [°C].

Equation (2) models how the power generated by a photovoltaic panel varies as a function of cell temperature and incident irradiance.

$$P_{\text{MOD}} = P_N \cdot G_M \cdot \frac{(1 + \gamma \cdot (T_C - 25))}{G_{\text{STC}}} \quad (2)$$

where

- P_{MOD} is the module PV power [W].
- γ is the temperature coefficient of P_N [$\% \cdot ^\circ\text{C}^{-1}$].
- P_N is the nominal power of the photovoltaic module [W].
- G_{STC} is the irradiance under standard measurement conditions [$\text{W} \cdot \text{m}^{-2}$].
- G_M is the irradiance [$\text{W} \cdot \text{m}^{-2}$].

Finally, using Equations (1) and (2), the hourly power production of the PV plant is calculated using Equation (3).

$$E_{PV} = N_P \cdot P_{\text{MOD}} \cdot C_{\text{LOSS}} \cdot T_S \quad (3)$$

where

- E_{PV} is the hourly PV energy production.
- N_P is the number of PV modules of the plant.
- C_{LOSS} are the losses associated with the PV plant (p.u.).
- T_S is the time slot of 1 h.

The accumulation of losses is quantified with the C_{LOSS} coefficient of 13.4% [26–28].

Using Equations (4)–(7), the energy stored in the BESS in each hour is calculated, taking into account the constraints and its equivalent model.

To adequately represent the energy balance of the BESS, the power restrictions specified in Equations (4) and (5) must be taken into account. P_{MAX} is equivalent to $E_{B,MAX}$ since the maximum C-rate is 1.

The charging ($P_{BC,t}$) and discharging ($P_{BD,t}$) power of the storage system is P_{MAX} , which is equivalent to its capacity, since the maximum C-rate is 1. During the charging process of the BESS, the power constraint is determined by the difference between the production of the PV plant and the energy supplied to the grid. In the discharge process of the BESS, the power constraint is based on the difference between the energy supplied to the grid and the output of the PV plant.

$$P_{BC,t} = \begin{cases} P_{MAX} & \forall (P_{PV,t} - P_{GRID,t}) > P_{MAX} \\ (P_{PV,t} - P_{GRID,t}) & \forall (P_{PV,t} - P_{GRID,t}) \leq P_{MAX} \end{cases} \quad (4)$$

$$P_{BD,t} = \begin{cases} P_{MAX} & \forall (P_{GRID,t} - P_{PV,t}) > P_{MAX} \\ (P_{GRID,t} - P_{PV,t}) & \forall (P_{GRID,t} - P_{PV,t}) \leq P_{MAX} \end{cases} \quad (5)$$

where

- $P_{BC,t}$ is the effective charging power of the BESS at the current time (t) in W.
- $P_{BD,t}$ is the effective discharge power of the BESS at the current time (t) in W.
- P_{MAX} is the nominal power of the BESS in W.
- $P_{PV,t}$ is the photovoltaic power supplied at the current time (t) in W.
- $P_{GRID,t}$ is the power setpoint to be supplied to the electrical grid at the current time (t) in W.

The stored energy at the current time (t) is related to the stored energy at the previous time ($t - 1$) [29,30] according to Equation (6).

$$E_{B,t} = \begin{cases} E_{B,t-1} \cdot (1 - \sigma) - \Delta t \cdot \eta_{B,EF} \cdot \left(P_{PV,t} - \frac{P_{BC,t}}{\eta_{B,INV}} \right) & t \in \text{charging} \\ E_{B,t-1} \cdot (1 - \sigma) - \left(\Delta t \cdot \frac{P_{BD,t}}{\eta_{B,INV}} - P_{PV,t} \right) & t \in \text{discharging} \end{cases} \quad (6)$$

where

- $E_{B,t-1}$ is the capacity of the BESS at the previous time ($t - 1$) in Wh.
- $\eta_{B,EF}$ is the round-trip efficiency in p.u.

The efficiency ($\eta_{B,INV}$) of Equation (6) varies in the proposed model depending on the power supplied. The efficiency of the conversion in the inverter has been taken from the Battery Energy Storage inverter Ingecon Sun Storage datasheet 100TL [31]. Therefore, Table 1 shows efficiencies for significant operating points with respect to the nominal power of the inverter that have been taken.

Table 1. Main parameters of utility-scale inverters and BESS.

Inverter BESS (Ingecon 100TL)		BESS (TS-I HV 100)	
Parameter	Value	Parameter	Value
Euro-Efficiency	98.1%	Max C-rate	1 C
Efficiency ($0.2 \cdot P_N$)	98.5%	Energy ($E_{B,MAX}$)	96 kWh
Efficiency ($0.4 \cdot P_N$)	98.5%	Round-trip efficiency	Up to 98%
Efficiency ($0.6 \cdot P_N$)	98.5%	Self-consumption	5 W
Efficiency ($0.8 \cdot P_N$)	98.2%	DoD	100%
Efficiency (P_N)	98%		

Self-discharge is measured as the charge lost over time and limits the energy available in the battery. The internal chemical reactions that contribute to self-discharge are mainly quantified when the BESS is not used for long periods of time. Due to the daily use of the BESS, the effect of self-discharge can be considered insignificant since the manufacturer of

the BESS identifies 5 W of losses [32]. Therefore, self-discharge phenomena are ruled out in the proposed model.

Regarding Equation (6), some operational limits related to the storage capacity of the BESS are established, which are identified from Equation (7). Although the BESS manufacturer indicates a 100% depth of discharge [32], for safety, a depth of discharge of 90% is chosen ($DoD = 0.9$).

$$E_{B,t} = \begin{cases} E_{B,MIN} & \forall E_{B,t} < E_{B,MAX} \cdot (1 - DoD) \\ E_{B,t} & \forall E_{B,MAX} \cdot (1 - DoD) < E_{B,t} < E_{B,MAX} \\ E_{B,MAX} & \forall E_{B,t} > E_{B,MAX} \end{cases} \quad (7)$$

where

- $E_{B,t}$ is the energy stored in the BESS for each hour.
- E_B represents the energy exchanged in 1 h with the BESS in Wh. Positive if it is charging and negative if it is discharging.
- $E_{B,MAX}$ is the upper capacity limit of the BESS in Wh.
- $E_{B,MIN}$ is the lower capacity limit of the BESS in Wh.
- $E_{B,t}$ is the hourly charging or discharging energy of the BESS at the current time (t) in Wh.

2.4. Model Phases

In the simulation process, a time step (Δt) of 1 h has been adopted. Consequently, all equations described in this section are evaluated at hourly intervals.

PV forecasting can be categorized into physical models and data-driven models. Physical models use numerical weather prediction, which shows good performance for forecast horizons from several hours to six days [11]. To analyze long-term data, data-driven models are often used. Although the proposed algorithm is not based on machine learning, its approach is similar to data-driven models. It adopts a strategy that is based on the processing and analysis of historical data accumulated over an extended period. This approach is characterized by unraveling meaningful patterns and relationships within a dataset.

The algorithm in MATLAB is divided into two subsections to solve the problem, as shown in Figure 3.

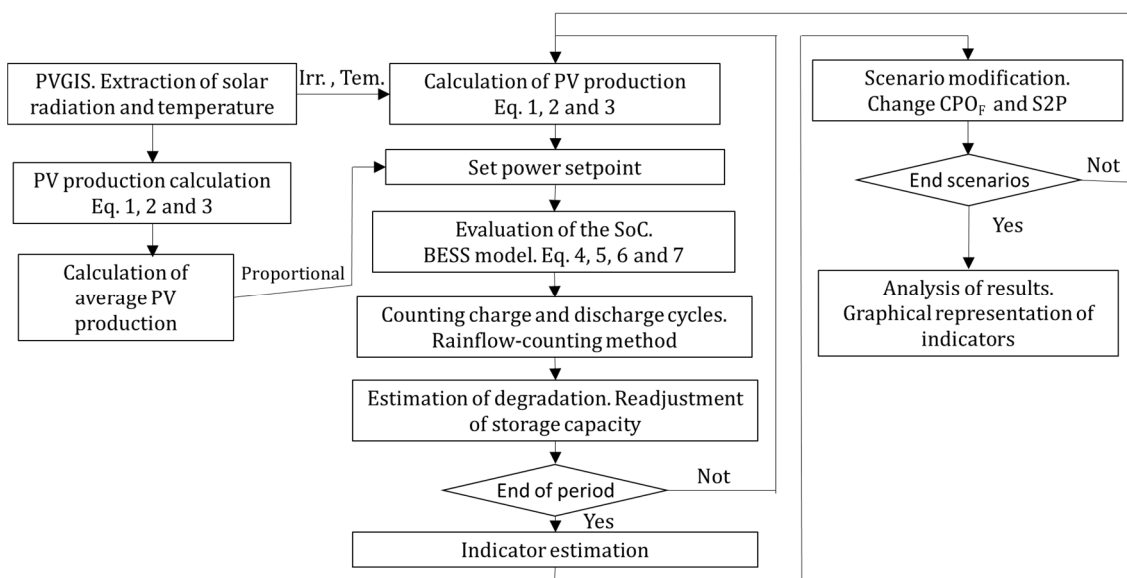


Figure 3. Model phases.

Left column blocks: As a preliminary step to the main simulation, a complete simulation of the time series is carried out using irradiance and hourly temperature as input variables. The hourly production of photovoltaic (PV) energy is determined for each hour of the simulation in order to calculate the average production of PV energy for each month of the year.

Center column blocks: The main simulation begins, in which, for each hour, the calculation of photovoltaic energy production is carried out based on the meteorological data provided by PVGIS. A constant power setpoint is established proportional to the average PV production of each month, obtained in the preliminary simulation. The SoC is calculated in the BESS according to its mathematical model. Charge and discharge cycles are counted by applying the rainflow-counting algorithm. Finally, the degree of degradation resulting from this cycling is estimated to adjust the capacity of the BESS. This process is repeated iteratively until the simulation is completed. At the end of the main simulation, the energy unavailability indicators are recorded. To identify significant operating points, the key parameters of the power setpoint and the size of the BESS are adjusted, thus repeating the main simulation. As a result, a matrix of indicators is generated based on parameters, which is used to graphically represent the results obtained.

2.5. System Parameters and Indicators

The specific parameters of the proposed BESS are provided in Table 2. This table lists the characteristics of the BESS, including the rated capacity, voltage, efficiency and expected lifetime according to data provided by the manufacturer [31].

Table 2. Parameters of the proposed BESS [32].

Parameter	Value
Nominal capacity	0–6 MWh
Rated Cycle-Life 1	6000 at 100% DoD and 1 C
Rated Cycle-Life 2	8000 at 100% DoD and 0.5 C
Operating voltage	845–1096 V
Cell Type	Lithium
Coulomb efficiency	98%
BESS inverter efficiency	96%

One of the most important characteristics of any electrical power system is its rated power, that is, how many kW it can produce on a continuous, full-power basis. If the system has a generator, the rated power is determined by the rated power of the generator. If the generator were to deliver its rated power for a full year, then the energy supplied would be the product of the rated power times 8760 h/year. Since power systems do not run at full power all year, they output less than the maximum amount. The capacity factor (CF) is a convenient, dimensionless quantity between 0 and 1 that connects the rated power to the energy delivered [33].

In Equation (8), the term CF represents the capacity factor, which is a dimensionless quantity between 0 and 1. E_{GRID} represents the energy supplied annually by the plant, while P_R is the rated power of the plant.

$$CF = \frac{E_{GRID}}{P_R \cdot 8760} \quad (8)$$

By the year of commissioning, the global weighted average capacity factor for new utility-scale solar PV reached 17.2% in 2021 [34].

The S2P parameter defines the storage capacity of the system according to Equation (9) [21]. C_{MAX} represents the storage capacity of the BESS in MWh, and P_P is the peak power of the

photovoltaic installation in MW. $S2P$ is a parameter equivalent to the number of hours of autonomy of a photovoltaic installation and is expressed in hours.

$$S2P = \frac{C_{MAX}}{P_P} \quad (9)$$

BESSs are designed to be versatile and easy to expand. The technical specifications for large batteries [32] detail the capacity of each storage module. Specifically, the TS-IHV100E storage module by Tesvolt Lutherstadt Wittenberg (Germany) has a capacity of 80 kWh and allows four modules to be connected in parallel in a cabinet (total of 320 kWh).

Assuming that an $S2P$ of 0.8 is to be selected and that the peak power of the PV plant is 1 MWp, the storage capacity of the BESS must be 0.8 MWh. This would require two full cabinets and an additional cabinet with two modules.

In Equation (10), the concept of the Constant Power Operating Factor is introduced [21]. P_{GRID} is the constant power that must be supplied to the electrical grid. This equation relates the power of the photovoltaic installation and the energy that must be provided to the grid. Therefore, the CPO_F parameter determines the equivalent operational performance of the system.

$$CPO_F = \frac{P_{GRID}}{P_P} \quad (10)$$

To ensure a constant and reliable energy supply, the system operation factor (CPO_F) must be lower than that associated with the average annual production of photovoltaic energy. If this requirement is not met, the photovoltaic installation will incur an annual energy deficit that the PV-BESS system cannot compensate. The CPO_F must be between 0 and 0.172 as mentioned for the average capacity factor previously. In Equation (11), the Annual Energy Deviation (AED) is defined as a relative accumulator of unavailable energy throughout the entire simulation period, where the numerator represents the unavailable energy, and the denominator represents the energy supplied throughout the entire simulation period [26]. E_{PV} represents the PV-BESS production for each hour, E_{GRID} represents the energy supplied each hour and h represents the number of hourly periods of the simulation. To obtain the average annual unavailability, the Annual Energy Deficit (AED) indicator will be used, which will take the average data of all simulation years.

In [35], in order to determine the firm capacity of a distributed generation, a specific method is used that aims to obtain the minimum expected return on an investment, taking into account a pre-established confidence level. In accordance with the criteria established in the said study, a confidence level of 95% has been determined. Therefore, this study aims to guarantee that 95% confidence level. This means that the AED indicator should not exceed 5%.

According to data provided by the U.S. Energy Information Administration (EIA), in the period between 2013 and 2022, the capacity factor of nuclear power plants in the United States ranged between 90.8% and 93.4% [6]. The guarantee of a 95% confidence level in the proposed PV-BESS equates its availability to that of a plant with the capacity to supply firm power in the electrical system.

$$AED = \frac{\left| \sum_{h=1}^{h=96360} (E_{PV} - E_{GRID}) \right|}{\sum_{h=1}^{h=96360} E_{GRID}} V(\sum_{h=1}^{h=96360} (E_{PV} - E_{GRID}) < 0) \quad (11)$$

The fundamental parameters of the BESS are evaluated primarily by Equations (12)–(14), presented in [36]. It is common to use the SoC and SoH to estimate the energy performance, while the C-rate is used to approximate power performance. The SoC represents the current capacity in the BESS and is defined by Equation (12), where Q_C is the content of the electric charge at the present state, and Q_{MAX} is the maximum electric charge storage capacity at the present state.

$$\text{SoC} = \frac{Q_C}{Q_{MAX}} \quad (12)$$

The SoH represents the state of health of the BESS and is defined by Equation (13), where Q_S is the maximum electric charge storage capacity in the specification, which indicates the fully charged battery capacity at the initial stage without degradation.

$$\text{SoH} = \frac{Q_{MAX}}{Q_S} \quad (13)$$

C-rate is a parameter to describe the charging and discharge speed, which is calculated in Equation (14) where I is the current.

$$C - rate = \frac{I}{Q_S} \quad (14)$$

2.6. BESS Degradation Modeling

2.6.1. Equivalent Cycle Estimation

As shown in Figure 3, it is necessary to incorporate a degradation model for the BESS based on the accounting of charge and discharge cycles. The methodology that is usually presented to predict the useful life of batteries is based on situations where an identical charge–discharge cycle is repeated throughout the useful life of the battery. However, in most applications, the cycles change dynamically over time. In applications such as energy storage with renewable generation, daily variations in surplus generation lead to variability in the cyclic depth of discharge [37].

To identify the operational behavior of the BESS, it is necessary to use a consistent method that adequately accounts for charge and discharge cycles.

The rainflow-counting algorithm has been widely used in research to analyze the fatigue and degradation of materials [38]. This method identifies the loading cycles of a material subjected to fluctuating loads during its useful life. The algorithm allows for evaluating the durability of a component by estimating the stress levels necessary to produce fatigue failure.

Battery degradation is a complex phenomenon composed of several chemical processes. However, an analogy can be established with the fatigue phenomenon in materials. In both cases, part of the degradation process occurs as a result of the successive application of loads.

The method was first proposed by Matsuisi and Endo in 1968 and follows the ASTM [39].

The algorithm counts the equivalent charge–discharge cycles from the time series corresponding to the state of charge (SoC) of the BESS [40]. To facilitate the understanding of the process, a theoretical explanation of the method has been combined with a fictitious example based on Figure 4.

The procedure is listed below:

1. Reduce the SoC curve to a sequence of peaks and valleys by identifying inversions in the slope of the time series. Figure 4a identifies the sequence of points from 0 to 9;
2. Set the initial state of the SoC as the starting point for counting. In Figure 4a, this is marked as point 0;
3. Identify two consecutive inflection points and calculate the range of the three segments affected by that inflection. Each segment R_i is identified by a line delimited by two points. The absolute value of the difference between the extreme values is the range of the segment. In Figure 4a, the inflection points are 1 and 2. The range of segment 1 is $R_1 = |P_1 - P_0| = 30$. The range of segment 2 is $R_2 = |P_2 - P_1| = 50$, and the range of segment 3 is $R_3 = |P_3 - P_2| = 30$;
4. A complete cycle is identified if the range R_i is less than the range before and after. $R_i < \min(R_{i-1}, R_{i+1})$. This condition is met in Figure 4c, where the range of segment S4 is smaller than in S3 and S5;

5. If the conditions of step 4 are met, eliminate the points associated with the range R_i and repeat the process from step 3. In Figure 4d, points 3 and 4 are eliminated;
6. If a complete cycle is not identified, proceed to the next points and repeat the process from step 3. In Figure 4a, segment S2 does not meet the identification of a complete cycle from step 4. It must be analyzed in the next segment (S3) in Figure 4b;
7. The cycle detection process is repeated until the remaining profile is completed;
8. Once all the complete cycles have been identified, the remaining segments are considered as half cycles. Segment S2 in Figure 4a and segment S3 in Figure 4b are half cycles of the series.

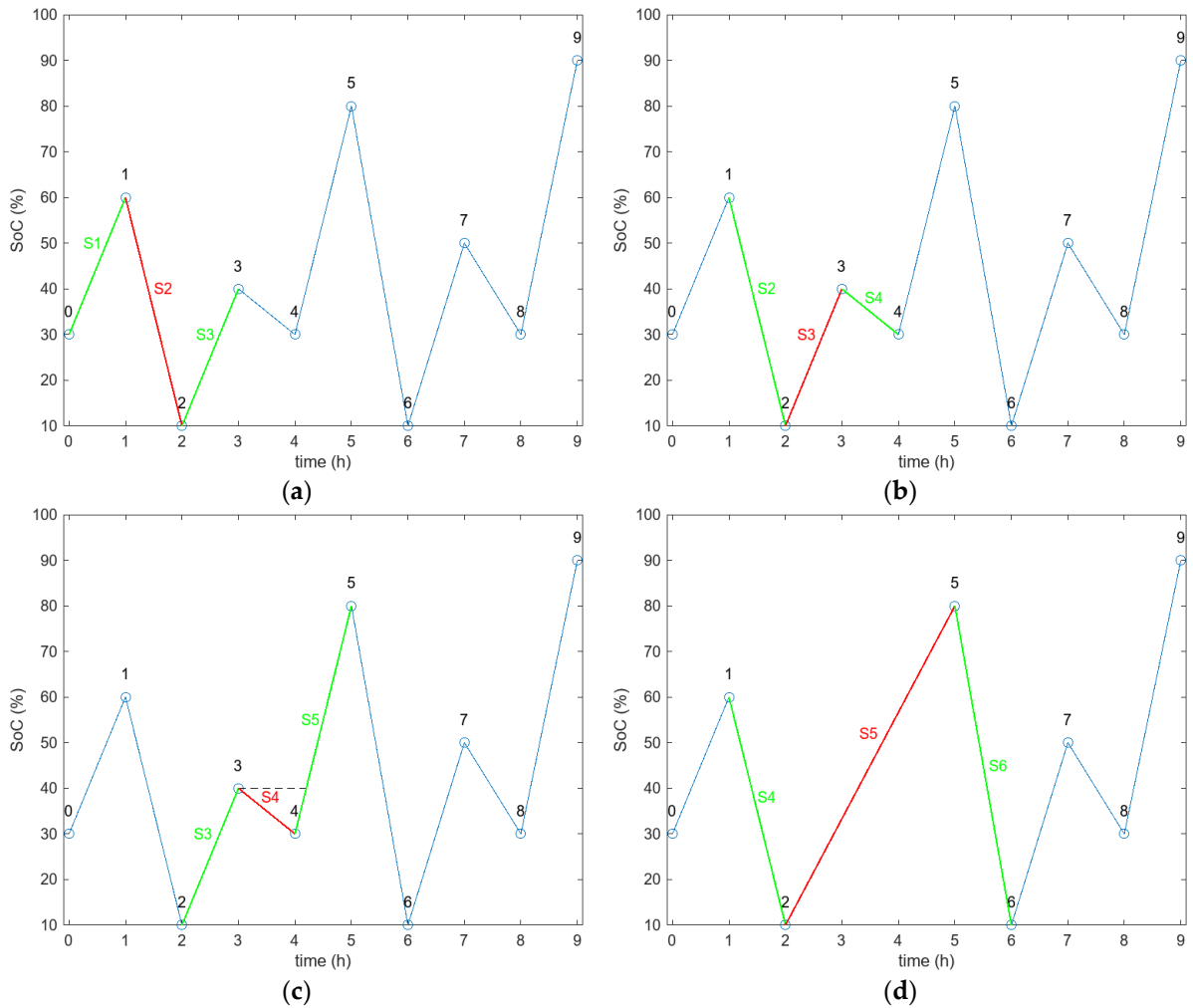


Figure 4. Example of rainflow-counting algorithm. (a) Half-cycle counting in segment S2; (b) half-cycle count in segment S3; (c) counting a complete cycle in segment S4; (d) half-cycle count after redoing points in the new segment S5.

Each semicycle or cycle is classified according to its magnitude. The parameters that identify each magnitude are the average value of the path and the discharge depth. These parameters are essential to analyze the useful life of the batteries.

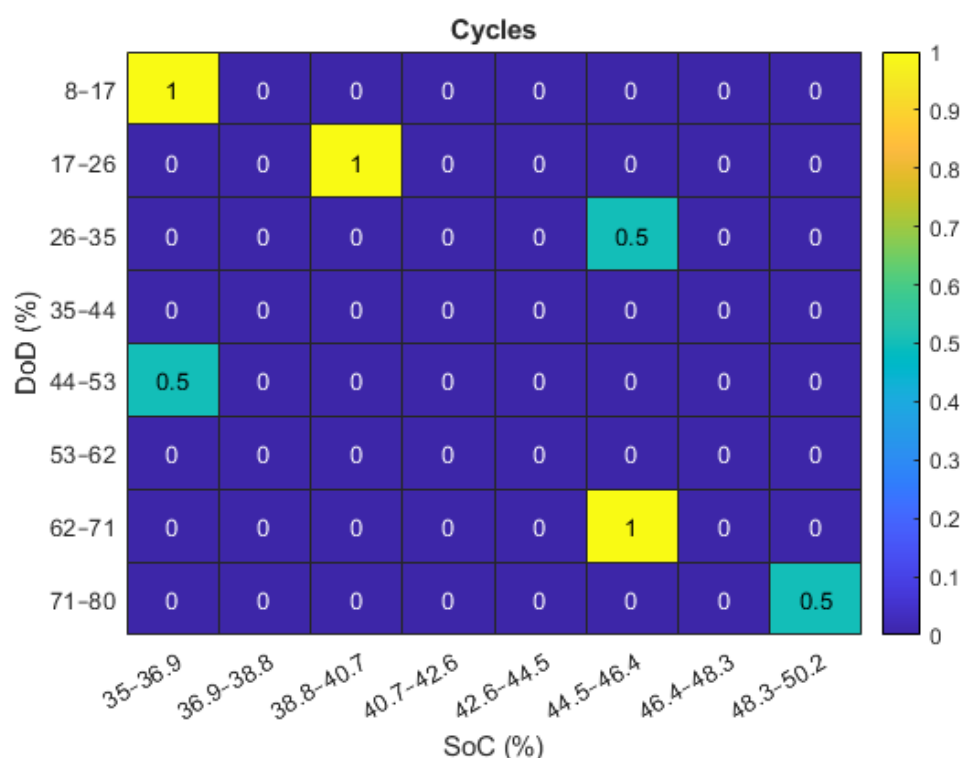
Table 3 shows all the half cycles or full cycles associated with the count in Figure 4. The count column identifies a half cycle (0.5) or complete cycle (1). The range column represents the discharge depth of the BESS. The mean column represents the average SoC of each half cycle or cycle. The start and end columns identify each segment in the timeline.

Table 3. Identification of sections in cycles and semicycles using the rainflow method for the proposed example.

Count	Range (%)	Mean (%)	Start (h)	End (h)
0.5	30	45	0	1
1	10	35	3	4
0.5	50	35	1	2
0.5	70	45	2	5
1	20	40	7	8
0.5	70	45	5	6
0.5	80	50	6	9

In summary, this algorithm computed in MATLAB that applies the rainflow method to the proposed fictitious case in Figure 4 has identified two cycles and five half cycles. The discharge depth and the average value of each section allow for a BESS degradation analysis to be carried out from a cycling point of view.

Figure 5 shows the number of equivalent cycles of the BESS as a function of the depth of discharge (DoD) and the average value of each cycle or half cycle, applying the rainflow-counting algorithm. The number of equivalent cycles is represented by a color scale, where yellow corresponds to a higher number of equivalent cycles. Each cell in the figure represents the number of equivalent cycles adjusted according to its amplitude and average value, since each component contributes a different weight to the BESS degradation.

**Figure 5.** The number of equivalent cycles according to the rainflow-counting method as a function of the depth of discharge (DoD) and average value (average) of the BESS.

In the simulations carried out in this study, the rainflow-counting algorithm is used to quantify the charge and discharge cycles in the battery.

In the Results section, cycling maps will be presented, similar to the example illustrated in Figure 5, which classify and provide a concise visualization of the distribution of charge and discharge cycles throughout the entire simulation.

Previous experimental research has shown that deep cycling causes the most significant degradation, whereas smaller cycles are less significant [37]. Thus, to achieve an accurate quantification of BESS degradation, it is necessary to determine the number of cycles for each level of discharge depth. Each segment represented in Figure 5 generates a different level of degradation that will be quantified below.

2.6.2. Degradation Model of BESS

Batteries are electrochemical devices used to store and supply electrical energy. Due to the nature of their chemical composition, they are subject to a degradation process. The design, the electrochemical system, the temperature, the type of discharge and the storage period are factors that affect the useful life of batteries [26].

There are different approaches to degradation modeling to quantify aging. Empirical models are based on data obtained through tests, semi-empirical models are based on data from aging studies and physicochemical models model aging mechanisms exclusively with differential equations. The simulations proposed to analyze the degradation in this paper are based on an empirical model supported by the tests carried out in [41,42].

Battery degradation is attributed to two independent components, known as cycling aging and calendar aging. In Equation (15), the term D_{TOT} represents the total degradation, while D_{CAL} represents the degradation attributable to calendar aging, and D_{CYC} represents the degradation related to the battery charging and discharging processes.

$$D_{TOT} = D_{CAL} + D_{CYC} \quad (15)$$

The factors that can influence each component are listed below.

Cycling Aging

To describe the degradation resulting from charge and discharge cycles, the term cycling aging is used. The main factors that contribute to increased degradation due to cycling aging are listed below.

Temperature (T): High temperatures cause cathode degradation and volume expansion, which accelerates the growth of the solid electrolyte interface (SEI) on the anode. Both causes are associated with a decrease in capacity and an increase in internal resistance [43]. The Arrhenius equation states that the rate of a chemical reaction increases exponentially with temperature [41]. Using Equation (16), the coefficient that relates temperature to degradation (K_{CYC-T}) is modeled. K_T is a parameter determined by empirical methods [41], T_R is the reference temperature of 25 °C and T is the ambient temperature.

$$K_{CYC-T}(T) = e^{k_T \cdot (T - T_R) \cdot \frac{T_R}{T}} \quad (16)$$

Average state of charge (\overline{SoC}): The (\overline{SoC}) of a charge–discharge cycle has a slight influence compared to other factors such as the depth of discharge (DoD). In [44], results are presented that indicate that carrying out cycling at high SoC ranges results in a significant loss of active lithium. This is due to the considerable expansion experienced on the surface of the graphite particles at a high SoC during the transition between the lithiation stages. As a consequence, the SEI layer on the surface breaks down and rebuilds itself irreversibly, leading to the consumption of active lithium. The relationship between this degradation coefficient ($K_{CYC-SOC}$) and the SoC is modeled by Equation (17). K_σ is a parameter that characterizes the sensitivity of the degradation determined in this equation.

$$K_{CYC-SOC}(\sigma) = e^{k_\sigma \cdot (\sigma - \sigma_R)} \quad (17)$$

Depth of discharge (DoD): It represents the difference between the SoC levels reached during a charge or discharge half cycle. It has been observed that as the degree of discharge (DoD) increases, more degradation occurs. High discharge values imply a greater risk of cracking and the formation of a new solid electrolyte interface (SEI) layer due to volume

expansion in the graphite anode, especially when crossing the phase change regions in the anode [44]. Empirical methods, such as [35] and [41], propose degradation models as a function of the DoD using exponential functions. In Equation (18), $K_{CYC-DOD}$ represents the degradation coefficient as a function of the DoD, where K_{BAT} is the degradation constant provided by the manufacturer, δ is the DoD and $K_{\delta 1}$ is a parameter identified empirically in [45].

$$K_{CYC-DOD}(\delta) = (K_{BAT} \cdot \delta)^{K_{\delta 1}} \quad (18)$$

The K_{BAT} degradation constant can be obtained from the data provided by the manufacturer. In Equation (19), D_{EoL} represents the degradation per unit expected at the end of the useful life of the batteries (approximately 0.8), while N_{CYC} corresponds to the number of cycles necessary to reach this degradation.

$$K_{BAT} = \frac{D_{EoL}}{(N_{CYC} \cdot (1 - D_{EoL}))^{K_{\delta 1}}} \quad (19)$$

Number of equivalent cycles (NEC): Charging and discharging a battery does not always start with a 100% state of charge (SoC) and end at 0% SoC, which would represent a full cycle. The NEC for a given DoD is defined as the number of cycles equivalent to a scenario where a full charge or discharge is performed in each cycle. The most pronounced aging mechanism is attributed to battery cycling, which involves graphite exfoliation, structural decomposition, transition metal dissolution and the growth of the solid electrolyte interface (SEI) layer. As a result of the factors explained above, the cycling aging component is obtained using Equation (20).

$$K_{CYC} = K_{CYC-T}(T) \cdot K_{CYC-SOC}(\sigma) \cdot K_{CYC-DOD}(\delta) \quad (20)$$

The resulting degradation does not follow a linear relationship. In order to fit the behavior of real cycling aging to the model proposed in this article, Equation (21) is used, which applies a non-linear relationship. K_1 and K_2 are the constants identified in [41] to fit the model. The rainflow-counting algorithm method used is essential for quantifying the degradation due to cycling, since it provides information on the average value of the SoC, the DoD and the NEC.

$$D_{CYC} = 1 - K_1^{-K_2 \cdot K_{CYC} \cdot NEC} - (1 - K_1)^{-K_{CYC} \cdot NEC} \quad (21)$$

Calendar Aging

The aging effects due to storage or the period of inactivity of the battery are called calendar aging. These effects are related to the loss of capacity due to the passage of time and are not independent of the charge and discharge cycles [42]. The estimation of the degradation caused by the chemical decomposition of the electrolyte solution is clearly identified. Below are the factors that intensify the degradation related to calendar aging.

Temperature (T): Elevated temperature leads to the faster growth of the solid electrolyte interface (SEI) layer. This phenomenon accelerates cell degradation [46]. The K_{CYC-T} factor of Equation (16) is valid to model this behavior.

Time (t): Reactions due to SEI growth and binder decomposition increase over time. Even in the absence of charge and discharge cycles, the degradation mentioned in [46] occurs. The K_t factor of Equation (22) models this behavior by taking the constant K_{C1} through empirical tests in [41].

$$K_t = K_{C1} \cdot t \quad (22)$$

State of Charge (SOC): If the battery charge level is high, there is a low potential at the anode and a high potential at the cathode. As mentioned in [46], this low potential at the anode accelerates the growth of the SEI, resulting in the acceleration of the degradation. Furthermore, the oxidation of lattice oxygen is an electrochemical process that occurs mainly at high state of charge (SOC) ranges. This process results in a greater dissolution

of the transition metal due to the oxidation of the lattice oxygen of the cathode [47]. The $K_{CYC-SOC}$ factor of Equation (3) is valid for modeling this behavior. As a result of the factors explained above, the calendar aging component is obtained using Equation (23).

$$K_{CAL} = K_{CYC-T}(T) \cdot K_{CYC-SOC}(\sigma) \cdot K_t \quad (23)$$

As in cycling aging, for calendar aging, the degradation does not follow a linear relationship. To adjust the behavior, Equation (24) is used, which applies a non-linear relationship.

$$D_{CAL} = (1 - K_1)^{-K_2 \cdot K_{CAL}} - (1 - K_1)^{-K_{CAL}} \quad (24)$$

Table 4 presents the parameters used to identify the proposed degradation model, which are obtained from experimental results taken from [41,45,48].

Table 4. Degradation equation parameters.

Name	Value	Equation
K_T	0.0693	2
T_R	25 °C	2
K_σ	1.039	3
σ_R	0.45	3
$K_{\delta 1}$	2.03	4 and 5
K_1	0.0575	7
K_2	121	7
K_{C1}	4.14×10^{-10}	8

2.6.3. Issues with Lithium-Ion Batteries

The main limitations of lithium-ion batteries are the high price, lack of lithium supply and safety issues related to electrolytes.

The review article [49] presents the main issues discussed in the literature on lithium-ion batteries. They are summarized below:

- Increasing temperature has a significant impact on the accuracy of methods used to estimate the state of health, as well as increasing degradation in cells;
- It is essential that proper heat dissipation methods are implemented in batteries. Failure to do so can result in reduced battery life, poor cycling performance and an increased risk of explosion;
- Chemical separation processes for recycling face significant challenges on a large scale. Ethical and environmental concerns arise in the extraction of lithium, cobalt and other mineral resources, as well as issues related to their safe disposal;
- Despite the efforts made in the research of cathodes, anodes and electrolytes, significant challenges remain. These include cathode dissolution, the negative effect of electrostatic interaction, dendrite formation, corrosion and passivation. These difficulties can lead to significant capacity degradation, low efficiency and short circuits;
- Interface stability is a challenge because excessive overcharging or discharging, together with short circuits, causes cells to charge or discharge unevenly.

3. Results

The simulations carried out with constant power setpoints up to Section 3.4 have been configured to maintain an intermediate value ($CPO_F = 0.1$). In [21], simulations were carried out using various power setpoints, and it was identified that a CPO_F of 0.1 achieves an appropriate balance between the amount of energy supplied to the grid and viable energy unavailability, without the need to significantly oversize the BESS. If all the energy produced by the PV plant could be supplied, the capacity factor would be equivalent to the CPO_F power setpoint. In the Introduction, statistical data have been provided indicating that the average capacity factor in PV plants is 0.172. Therefore, it would not be feasible to

supply power setpoints that exceed this value, and a setpoint with a CPO_F of 0.1 is a value close to the intermediate value.

In Section 3.1, an initial approach is carried out to analyze the influence of each parameter on the degradation in the BESS.

In Section 3.2, using the rainflow-counting algorithm, the model proposed in this study is simulated in order to analyze how degradation affects the cycling distribution in the BESS. The gradual degradation of the BESS has a significant impact on the fundamental degradation variables, which are the DoD and the \overline{SoC} .

After analyzing the influence of each parameter on the degradation and distribution of cycles in the simulation, starting in Section 3.3, results such as the predicted EoL and energy unavailability are presented. The purpose is to determine an appropriate installation size, taking into account variations in S2P and CPO_F .

3.1. Influence of Degradation according to its Parameters

The equations formulated in Section 2.6 provide a mathematical framework to quantify the degradation experienced by a BESS due to cycling and calendar aging.

In this section, a simulation of the proposed model is carried out to analyze the influence of calendar aging and cycling. The results obtained confirm the validity of the model and ensure that the degradation is correctly estimated in subsequent simulations.

To achieve this, theoretical scenarios are simulated in which charges and discharges are applied to the storage system following cyclic patterns. The graphical results are shown in Figures 6 and 7, where the state of health due to cyclic aging is identified. On the other hand, Figure 7 shows the state of health due to calendar aging.

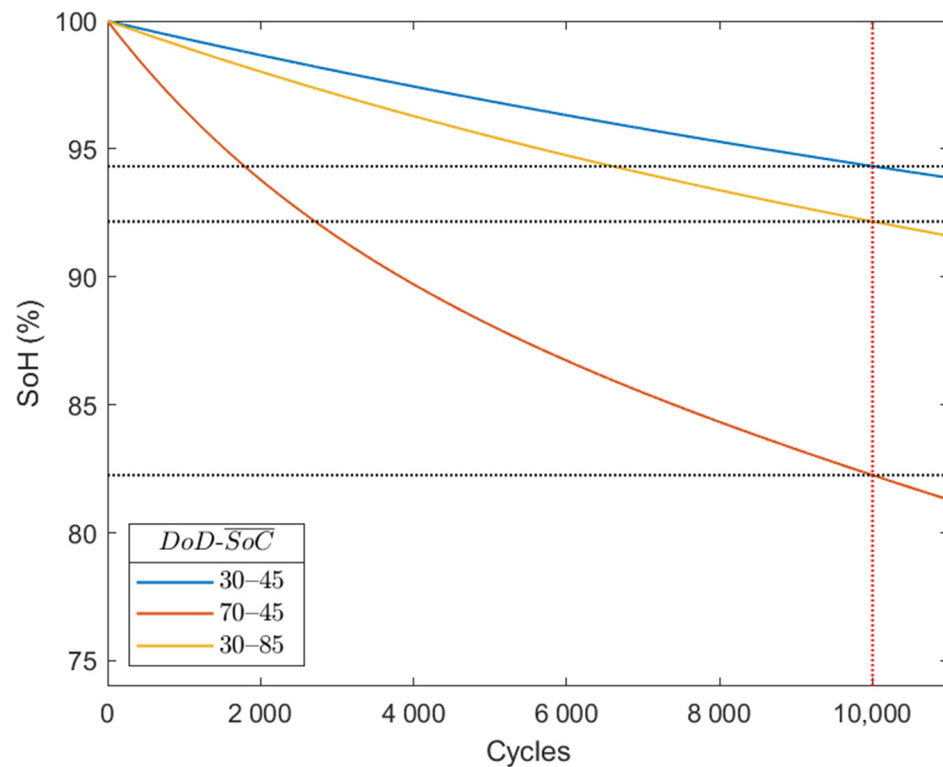


Figure 6. BESS cycling degradation curve for different DoD and \overline{SoC} .

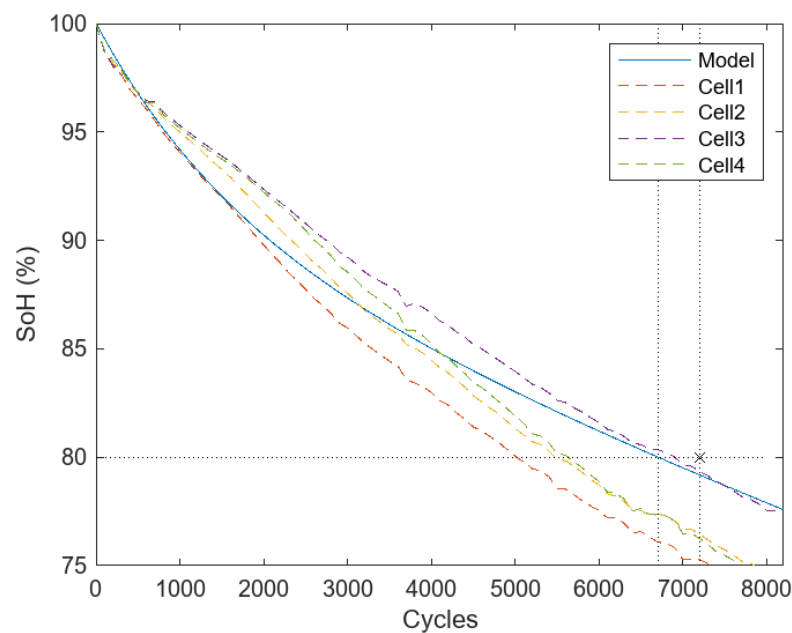


Figure 7. BESS cycling degradation curve of the proposed model with respect to the degradation of real batteries.

3.1.1. Cycling Aging influence

A simulation is carried out in MATLAB using the proposed model in order to analyze the influence of its main variables, the DoD and \overline{SoC} . In this theoretical scenario, the variables DoD and \overline{SoC} remain constant throughout the simulation, which implies that periodic charge and discharge cycles with identical magnitudes are performed. A constant temperature of 25 °C is assumed, to make the temperature variable independent of aging. The results obtained identify the influence of each variable on the gradual loss of battery capacity with each cycle.

Figure 6 shows a comparison of the SoH up to 10,000 cycles, for three cases with different cycling.

The blue curve in Figure 6 is taken as a reference, with a DoD of 30% and \overline{SoC} of 45%. In this system, symmetrical charges and discharges are carried out in the range of SoC values from 30% to 60%. The simulation corresponding to the blue curve in Figure 6 modifies each variable with an increase of 40% to analyze which of them has a greater influence on the degradation.

In the first case, the orange curve in Figure 6 represents a simulation in which the DoD is increased by 40% with respect to the blue reference curve. Symmetric charges and discharges are carried out in the range of SoC values ranging from 10% to 80%. Since this curve shares the same \overline{SoC} as the blue curve, it isolates the influence of the \overline{SoC} and facilitates the verification of the significant relationship between the degradation and the depth of discharge. The SoH after 10,000 cycles in the blue reference curve is 94.32%, and by increasing the DoD by 40% in the orange curve, the SoH drops to 82.25%. These results support the hypothesis that the DoD has a substantial impact on the degradation phenomena mentioned in Section 2.6.

In the second case, the yellow curve in Figure 6 with a DoD of 30% and \overline{SoC} of 85% represents a simulation in which the \overline{SoC} is increased by 40% with respect to the blue reference curve. The system performs symmetrical charges and discharges in the range of SoC values ranging from 70% to 100%. Only the \overline{SoC} has been modified in comparison with the simulation of the reference blue curve, thus allowing for the influence of the \overline{SoC} to be analyzed. The SoH after 10,000 cycles in the blue reference curve is 94.32%, and by increasing the \overline{SoC} by 40% in the yellow curve, the SoH only drops to 92.16%.

The conclusion drawn is that the influence of the DoD is more significant than that of the \overline{SoC} but both must be taken into account for the cycling degradation analysis.

To estimate the degradation, it is common to propose a cycling aging model based on the DoD and \overline{SoC} variables, using the rainflow-counting algorithm for cycle counting [28,33].

To validate the proposed cycling aging model, it is compared with long-term aging tests of lithium batteries. An industry reference dataset from the Oxford University Research Archive [44,50] is used. This dataset contains a long-term battery aging test for lithium-ion cells.

Figure 7 shows a graphical representation of the SoH or degradation as a function of the number of battery cycles. The blue curve with a solid line corresponds to the proposed model, while the curves with dashed lines represent the degradation of four types of batteries in the dataset [44,50].

It can be seen that the degradation levels in Figure 7 are comparatively similar, although not identical. It is complex to identify an exact degradation pattern for each battery. Based on this observation, it is considered that the proposed model has substantial validity in predicting the degradation process until the End of Life or a SoH of 80%.

To validate the experimental model, a comparison is made with the data provided by the manufacturer of a commercial battery. The Lithium Iron-Phosphate PowerBrick battery datasheet [51] presents the number of cycles vs. depth of discharge graph. For the curve with a DoD of 90% and a C-rate of 0.25 C, which resembles the average value of the proposed simulation, 7200 useful life cycles are identified.

According to the manufacturer's specifications, the service life of the battery is considered to cover up to 80% of the initial capacity. Therefore, in Figure 7, the End of Life according to the manufacturer has been identified with an "x".

In the proposed model, the intersection between the limit value of 80% and the blue "model" curve in Figure 7 identifies 6700 equivalent cycles, which is similar to the real value provided by the manufacturer. The data are compared with a Lithium Iron-Phosphate battery, because the composition of this type of battery has been used in large-scale BESSs such as [32].

3.1.2. Calendar Aging Influence

The equations formulated in Section 2.6 on calendar aging allow for the degradation to be quantified, considering both the passage of time and the SoC value. Several simulations are carried out in order to validate the proposed model, assuming that there is no cycling of the battery and the charge level is kept constant.

Figure 8, with the legend "sim", shows the calendar aging caused by the proposed model. Compare with a degradation dataset obtained in [52] whose legend in Figure 8 is "test".

Note that the higher the average state of charge \overline{SoC} , the greater the degradation. After 2.5 years, the calendar aging simulation estimates a SoH of 88% when the SoC is 100%. However, the SoH is 91% when the SoC is 40%, as shown in Figure 8.

To corroborate the aging calendar, degradation data of a lithium-ion storage system are presented in [53]. It is observed that the degradation experienced coincides with that represented in Figure 8 after approximately 2 years. For an SoC of 40%, an SoH of 92% is reported in [53]. This figure coincides with the value represented in Figure 8, where it is also observed that for an SoC of 40%, there is an SoH of the order of 92%. For an SoC of 100%, the SoH in both cases is around 90%.

Another relevant aspect is that the calendar aging is more pronounced during the first years of the battery's life. The simulations represented in Figure 8 coincide in showing a higher level of degradation around the first year.

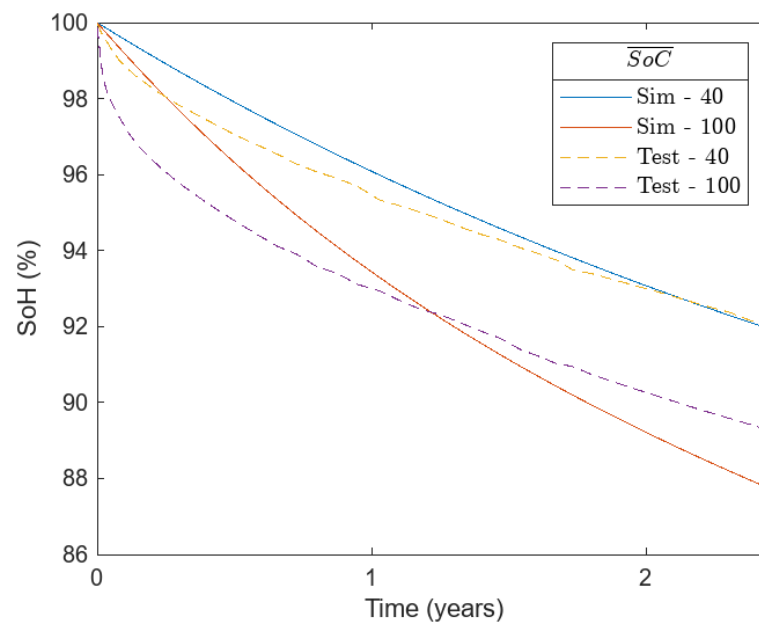


Figure 8. Calendar degradation curve in the proposed model with respect to real batteries for different \overline{SoC} .

In addition, a comparison of this model with a commercial battery is carried out. Taking the Lithium Iron-Phosphate PowerBrick battery [51] as a reference, the manufacturer establishes in its specifications a calendar life greater than 10 years. Therefore, upon the expiration of this period, the End of Life is considered to have been reached, which results in a reduction in the storage capacity to 80%. In other words, the degradation is estimated to be equivalent to 20%.

For the equations proposed in the model of this article, the projection of an SoC of 80% would reach an End of Life at 8.7 years and for an SoC of 60%, at 10.7 years.

Therefore, it can be concluded that the calendar life of the proposed model is consistent and similar to the manufacturer's specifications when average SoC values between 60 and 80% are considered.

3.2. The Influence of Degradation on the Cycling Distribution in the BESS

The introduction of degradation in the proposed model leads to a significant alteration of the BESS cycling process, since it causes a gradual decrease in its capacity. One of the most significant facts is the progressive degradation that affects the deeper discharge cycles, preventing them from reaching their maximum level. This implies that the BESS operation strategies are modified due to a capacity limitation.

Two simulations of the proposed model are carried out with the aim of analyzing its behavior until reaching the End of Life of the BESS, technically defined as 20% degradation in relation to its initial capacity.

3.2.1. Cycling Analysis for Reduced BESS Size

A relatively small storage size is chosen to ensure that the battery undergoes a full charge or discharge cycle in each operating cycle since its small capacity brings it to a state of full charge or discharge quickly. In this way, it is possible to systematically observe how high discharge depths, which are around 90%, experience a substantial reduction.

Figure 9 shows the behavior of the BESS through the analysis based on the count of load cycles (rainflow-counting algorithm). As observed in Section 2, the charge cycle count is an essential metric in the characterization of the BESS. Figure 9 provides a visual representation illustrating how each cycle occurs in the BESS.

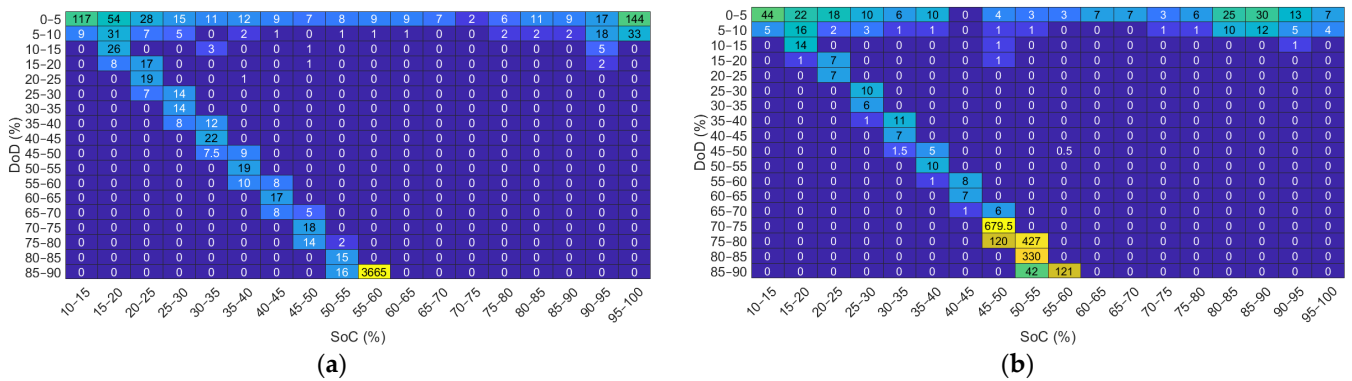


Figure 9. Rainflow-counting results for $CPO_F = 0.1$ and $S2P = 1$. (a) Without aging. (b) Aging until EoL.

Figure 9a shows a distribution of the charging cycles in which it is observed that the highest concentration of these cycles is around a DoD close to 90%. Additionally, the SoC is estimated at approximately 55%. Consequently, during each operating cycle, the system experiences a variation in the SoC that ranges between 10% and 100% of its total capacity. Specifically, the BESS has been subjected to 3665 operating cycles in this operating range. The rest of the cycles, compared to the magnitude mentioned, are numerically smaller and can be considered insignificant. This situation arises because the BESS has a relatively limited nominal capacity. Consequently, during any energy transfer process, whether charging or discharging, the BESS tends to reach its maximum capacity or be completely depleted. Figure 9b incorporates the aging until its End of Life, which occurs at 44,352 h. Only during the first operating cycles of the BESS is it possible to reach maximum depths of discharge of 90%. Due to the manifestation of degradation phenomena inherent to the use, the ability to reach such a DoD decreases. This development reflects the importance of considering aging phenomena in a BESS.

In Figure 9b, the aging phenomena are taken into account until its End of Life, which occurs at 44,352 h. It is only during the first operating cycles of the BESS that it is possible to reach maximum depths of discharge of 90%. Due to the manifestation of degradation phenomena inherent to the use, the capacity to reach such a DoD decreases. This development reflects the importance of considering aging phenomena in a BESS.

In Figure 9b, it can be seen that the dominant distribution of operating cycles has changed in relation to Figure 9a. Most of these cycles are now concentrated around 80% DoD and 50% SoC. It is noted that most DoDs start around 90% and decrease to around 70%. This indicates that, over the life of the BESS, it is operating in a DoD range that begins near its maximum capacity and gradually decreases over time as the battery degrades.

The observed situation has both positive and negative implications for the BESS. It is beneficial that, by operating with a smaller DoD, the phenomena of cycling aging are reduced. However, there is a progressive limitation on the capacity of the BESS. This restriction can lead to increases in energy unavailability in the system.

The degradation of the BESS constitutes a significant restriction in terms of its storage capacity, as observed in Figure 9, and, consequently, its effects are interesting to analyze in relation to the parameters of unavailability of reliable energy throughout the time.

To obtain a perspective of the evolution of the energy levels in the BESS in this simulation, Figure 10a is presented. The 3D graph illustrates the annual evolution of the resulting SoC during the operation of the BESS. It shows the day of the year on the “x” axis (day of the year), the sample number of each day on the “y” axis, which are the hours of the day, and the SoC on the “z” axis. In a small capacity battery, the SoC is fully charged and discharged most of the time. For days without PV production, the SoC remains fully discharged, as seen on day 8 of Figure 10b.

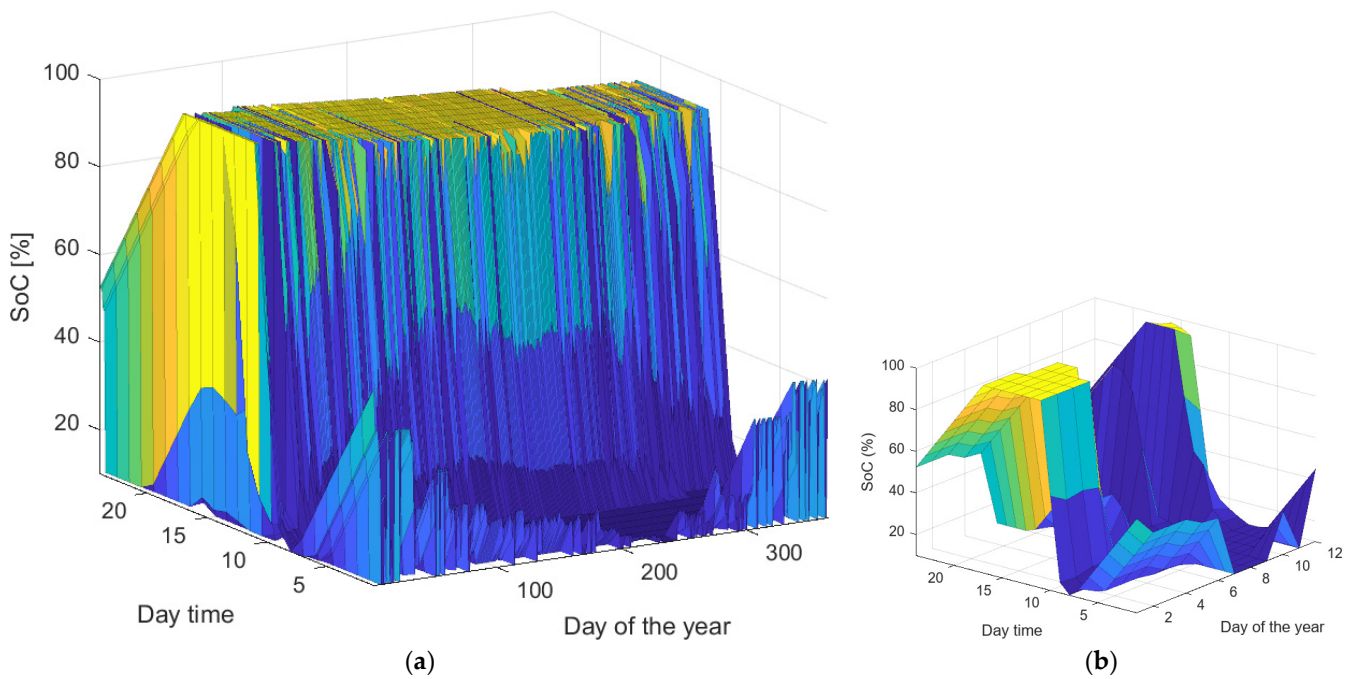


Figure 10. The evolution of the SoC in the first year of the simulation for S2P = 1. (a) Full year; (b) zoom in the first 12 days.

3.2.2. Cycling Analysis for Oversize BESS Size

Figure 11 shows the distributions of the load cycles associated with an oversized BESS (S2P = 5). This situation contrasts markedly with Figure 9.

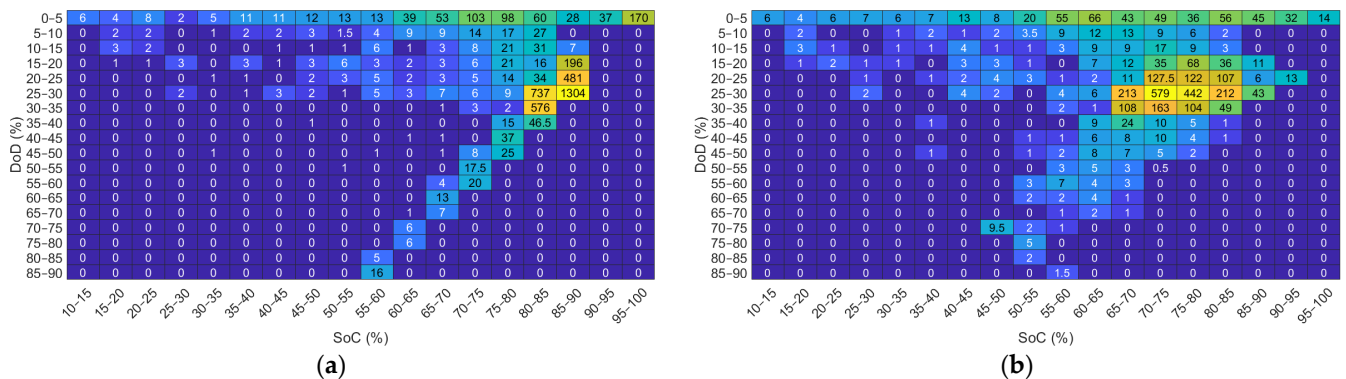


Figure 11. Rainflow-counting results for $CPOF = 0.1$ and S2P = 5. (a) Without aging. (b) Aging until EoL.

In a hypothetical context where BESS degradation was not a factor to consider, it is observed in Figure 11a that the majority of the cycles are concentrated around a relatively low DoD, approximately 30%. Additionally, the SoC remains at a high level, around 85%. Consequently, in each operating cycle, the system goes through fluctuations that range between 70% and 100% of its total capacity. These data suggest that, under these theoretical conditions, the BESS operates mostly in a higher range of its capacity, avoiding deep discharges and maintaining a high charge level. The rest of the cycles, compared to the magnitude mentioned, are numerically smaller and can be considered insignificant.

Figure 11b shows the aging phenomena until their End of Life, which occurs at 69,344 h. The dominant distribution of operating cycles has changed in relation to Figure 11a. Most of these cycles are concentrated for a DoD of 30% and a SoC ranging between 60% and 80%.

Although degradation phenomena reduce the storage capacity, the degradation tends to be mitigated since the \overline{SoC} is reduced. This suggests that over the useful life of the BESS, it is operating at a DoD of 30% and \overline{SoC} around 70%.

Figure 12 shows the evolution of the energy levels in the BESS for this specific case. Most of the time, the SoC is at levels close to 100%, and only occasionally after several days of low production does the SoC reach its minimum value, as can be seen in the zoom to Figure 12b.

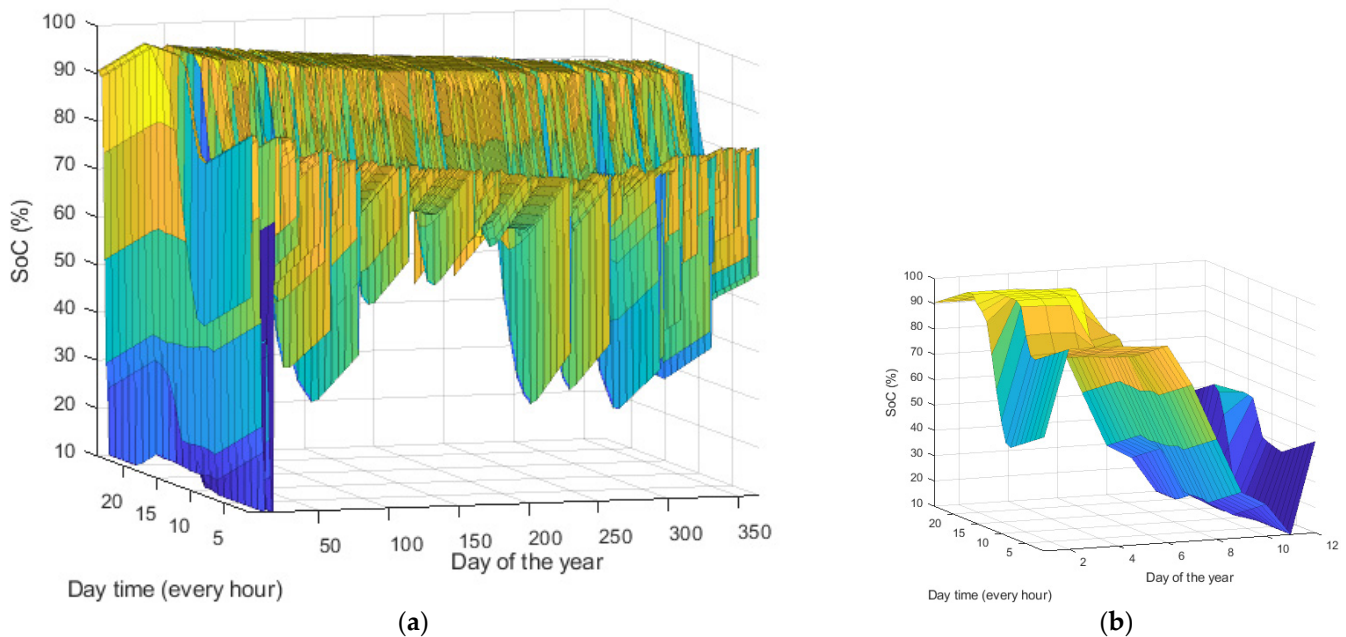


Figure 12. The evolution of the SoC in the first year of the simulation for $S2P = 5$. (a) Full year; (b) zoom in the first 12 days.

3.3. The Influence of the Size of the BESS on its End of Life

In the previous section, it was observed that the choice of BESS size has a significant effect on degradation. In order to determine the life of the BESS, the number of days until the BESS reaches the End of Life for each value of the $S2P$ indicator is presented in Figure 13a. This graphical representation provides information on how different BESS sizes affect system longevity.

In Figure 13a, it can be seen that when selecting an $S2P$ of up to 1.8, the degradation behavior is uniform, reaching the EoL approximately after 1875 days of operation. This specific feature is attributed to the limited storage capacity of the BESS. The storage system remains inoperative at its capacity extremes, either at maximum capacity due to a high PV generation or at its minimum capacity when there is no PV production, and the BESS is immediately discharged. It is important to highlight that these operating conditions are not valid in this study from the point of view of the energy unavailability of the system because the AED indicator exceeds 5%.

By increasing the storage capacity, and in particular when an $S2P$ value of 1.8 is exceeded, battery charging and discharging processes operate with a lower depth of discharge (DoD). This implies that, in each cycle, the BESS does not use its full capacity, which has a direct effect on reducing the degradation rate of the cells. Consequently, the durability of the system benefits from the point of view of the degradation due to cycling.

This relationship is clearly manifested in Figure 13a; as the $S2P$ increases beyond 1.8, the time to reach the EoL extends linearly.

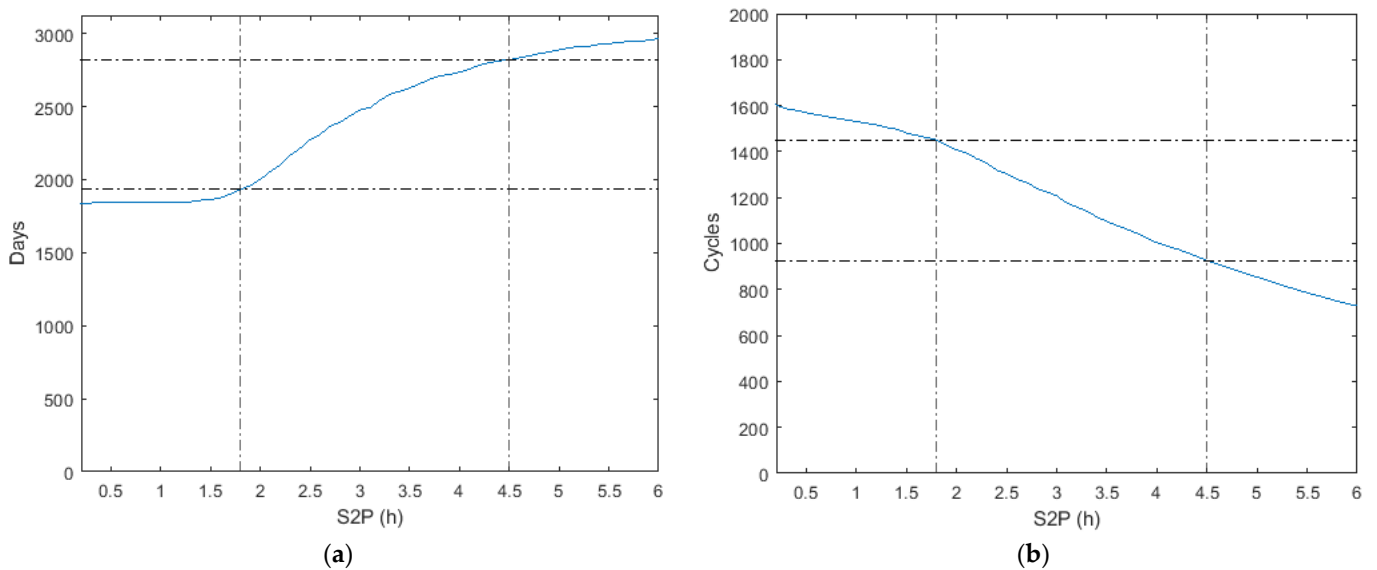


Figure 13. (a) Days to EoL as a function of S2P; (b) cycles to EoL as a function of S2P.

Starting from an S2P of 4.5, an inflection point is observed in Figure 13a. Beyond this value, the increase in time before reaching the EoL tends to plateau, regardless of how much S2P continues to increase. Having an excessively high storage capacity, the BESS is frequently subjected to slight charge and discharge cycles that produce low cycling degradation. Instead, the system mostly remains in a fully loaded state. This scenario with such a large S2P size is also not realistic, since it implies the excessive oversizing of the BESS.

When a larger storage is selected, a decrease is observed in the total number of cycles that the BESS performs until it reaches its EoL. As seen in Figure 13b, for a system with a more restricted capacity, specifically with an S2P of 1.8, the rainflow method, used to count charge and discharge cycles in storage systems, indicates that the BESS can support up to 1400 cycles equivalents up to their EoL. For a system with a larger storage capacity, with an S2P of 4.5, it presents an equivalent cycle reduction, supporting only 910 cycles until its EoL.

As mentioned in Section 2, the degradation of the BESS is due to calendar and cycling effects. In order to determine the specific influence of each of these effects in the analysis proposed in this section, Figure 14 shows the degradation curves corresponding to each of them as a function of the S2P parameter.

Figure 14 shows that calendar degradation increases with S2P. As the BESS capacity increases, it is observed that the SoC level remains high for longer periods of time. This behavior leads to further degradation per calendar. This correlation is corroborated with the calendar degradation study presented in Figure 8. In this study, it is observed that a higher state of charge (SoC = 100%) generates considerably greater degradation compared to a lower state of charge (SoC = 40%). The relationship between the BESS capacity, the duration of high SoC levels and the consequent degradation due to scheduling is coherently reflected in the results obtained, highlighting the direct influence that system capacity has on these effects.

In terms of cycling degradation, Figure 14 shows that an increasing S2P results in less degradation. This phenomenon is explained by the fact that a greater storage capacity implies charge and discharge cycles with a lower discharge depth. As previously discussed in Figure 6, the depth of discharge is the main factor in cycling degradation, and the lower it is, the lower the cycling degradation of the BESS. Therefore, it is confirmed that the behavior observed in this case coincides with the theoretical model previously analyzed in Figure 6.

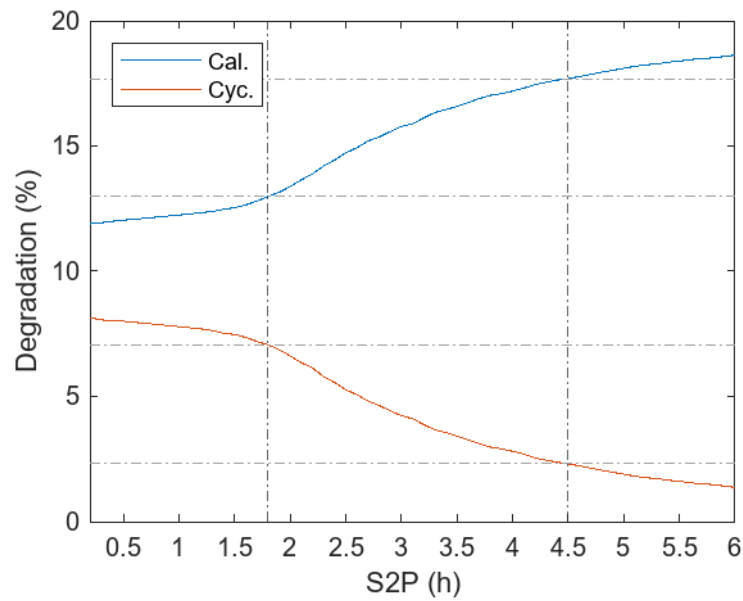


Figure 14. Calendar and cycling degradation until the EoL as a function of S2P.

Two sizes of BESSs are identified in Figure 14. A reduced storage capacity (S2P = 1.8) presents a degradation due to calendar aging of 13.1% and due to cycling of 7%. On the other hand, for a BESS with high storage capacity (S2P = 4.5), the degradation by calendar is significantly higher than that by cycling. By calendar aging it increases up to 17%, while by cycling it is reduced to 2.6%.

3.4. Selection of BESS to Guarantee High Availability of Firm Power

The AED indicator, used in studies [21,22], has made it possible to quantify energy unavailability in a system similar to the one proposed in this work.

The curves in Figure 15 show that there is a range of suitable storage sizes that guarantee the minimization of energy unavailability. The restriction is imposed that the AED indicator should not exceed 5%.

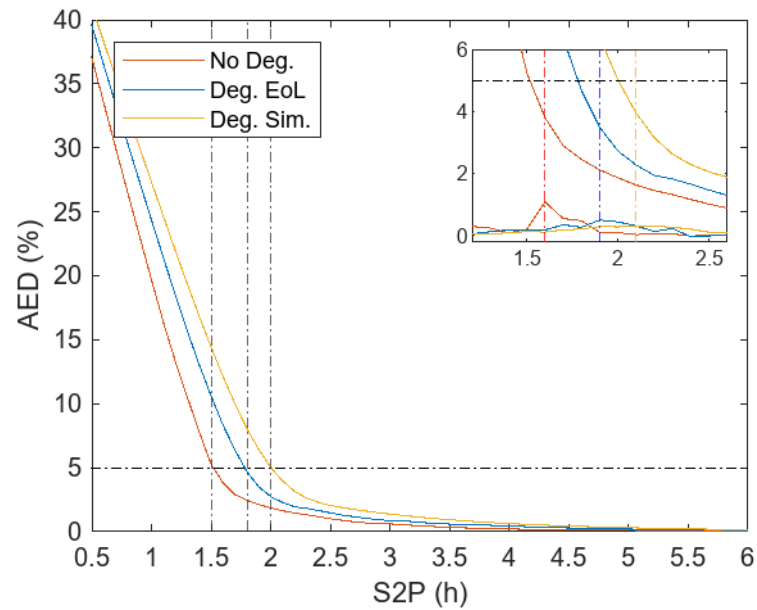


Figure 15. AED until EoL with and without degradation, and AED until end of simulation based on S2P.

In order to examine the effect of degradation on the AED indicator, several scenarios have been presented in Figure 15. The “No Deg.” curve, colored in red, simulates a hypothetical scenario in which the BESS operates without any degradation throughout its useful life until the End of Life. The “Deg. EoL” curve, represented in blue, reflects a more realistic scenario where the system experiences degradation until the End of Life.

The results obtained demonstrate that, to ensure an energy unavailability of less than 5%, a BESS with a capacity of $S2P = 1.5$ would be adequate in the theoretical scenario without degradation. However, when considering a realistic system of degradation in storage systems, it is necessary to increase the capacity to a value of $S2P = 1.8$ in order to reach the same threshold of energy unavailability. Consequently, it is significant that it is necessary to increase the storage capacity by 20% when taking into account the degradation phenomena in the BESS. This contrast underscores the importance of incorporating degradation factors in the design and sizing of BESSs.

It is commonly accepted to replace storage systems when they reach their EoL and the degradation reaches 20%. However, as the primary purpose of the PV-BESS is to ensure a constant power supply with low unavailability ($AED < 5\%$), it is advisable to consider the possibility of slightly oversizing the BESS by extending its useful life. This oversizing, as illustrated in Figure 13, involves increasing the S2P parameter and extends the time period until the EoL is reached. At the same time, this oversizing compensates for the gradual decrease in capacity due to degradation.

In Figure 15, the blue curve, labeled “Deg. EoL”, shows how the AED rate behaves in a simulation until reaching the end of the BESS useful life of 44,352 h. On the other hand, the curve in yellow, called “Deg. Sim.”, represents the AED index for the complete simulation, which covers a total of 96,432 h.

Selecting a value of $S2P = 1.8$ is considered appropriate to ensure that unavailabilities are less than 5% until the BESS EoL is reached. However, as seen in Figure 15, oversizing the BESS with a value of $S2P = 2$ ensures that the AED index remains below 5% throughout the simulation period, thus prolonging the useful life of batteries beyond the EoL. Specifically, this strategy extends the useful life from 44,352 h to a total of 96,432 h.

Additionally, Figure 15 shows a saturation zone beyond which increases in storage capacity do not lead to substantial reductions in unavailability. Therefore, the choice of the S2P parameter must be made before reaching the saturation point to optimize the selected storage size.

For the particular case proposed in Figure 15, the choice of S2P must be carried out in a way that guarantees that the unavailability (AED) remains below 5% at the end of the saturation elbow.

At the bottom of the zoom box in Figure 15, the second derivatives of the curves are plotted to highlight possible significant changes in the trend. The second derivative provides details about the concavity of the function. Therefore, the S2P value is chosen at which the maximum of each of these derivatives is reached, since this indicates a change in the trend.

The choice of S2P is optimized to ensure that unavailability remains below 5%. For a simulation up to the EoL, a value of $S2P = 1.9$ is required. However, if you are looking to prolong the life of the batteries, you could consider selecting a value of $S2P = 2.1$, as long as no failures occur in the batteries, since beyond the EoL, the manufacturer does not guarantee its correct functioning.

This strategy of prolonging the useful life of the batteries is presented as an innovative and risky choice, although valid, in terms of achieving reduced unavailability while optimizing the size of the BESS.

3.5. The Influence of the Power Setpoint on the Selection of the BESS with Degradation

In order to analyze the behavior of the AED indicator and determine the appropriate size of the BESS for different power setpoints, a comparison of three different scenarios is carried out. The first is a case of reduced power supply ($CPO_F = 0.04$) to guarantee high

energy availability for the system. The second is a case with a high power supply close to the maximum capacity factor that a PV plant can provide ($CPO_F = 0.16$). The third case is the one proposed in the previous subsection ($CPO_F = 0.1$) as a reference to compare results.

In Figure 16, two different curves are presented for each scenario analyzed. One curve represents the theoretical situation without degradation effects, while the second incorporates the degradation effects proposed in this study. For ease of identification, the curve reflecting the degradation is labeled with the letter “D” in the legend of Figure 16.

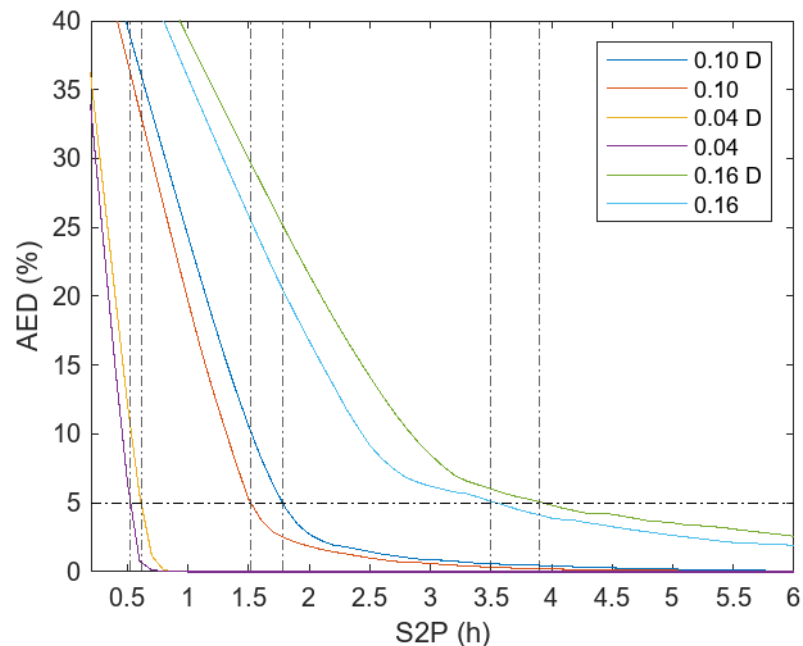


Figure 16. AED as a function of S2P for various CPO_F with and without aging.

In order to guarantee that the PV-BESS complies with energy unavailability of less than 5% for a CPO_F of 0.04, it can be seen in Figure 16 that the case without degradation requires an $S2P = 0.5$. However, when considering degradation phenomena, it is necessary to increase S2P to 0.62, which implies an increase in storage of 24%. For a CPO_F of 0.1, it is necessary to increase S2P from 1.5 to 1.8 when including degradation effects, which implies a 20% increase in S2P. For a CPO_F of 0.16, it is necessary to increase S2P from 3.5 to 3.85 by including the degradation of the BESS, which represents an increase of 10%.

Consequently, it is significant to highlight that as the power setpoint supplied by the system increases, the influence of degradation decreases. This implies that it is necessary to oversize the BESS less to meet the proposed energy availability objective.

4. Conclusions

The high cost of storage systems continues to be a gap in the academic literature when investigating PV-BESS hybrid plants operating with a constant power supply. However, the falling price of storage systems could make this configuration viable.

This study focuses on the energy aspect, using a realistic model that includes the detailed degradation effects of storage. Although this research focused on a specific case, the results can be extrapolated to any scenario with storage systems combined with photovoltaics.

Simulations have assessed the degradation of the BESS and its significant impact on storage capacity. This degradation has a direct impact on cycling operations. Comparing the proposed model with and without the degradation, it is found that it is necessary to increase the storage capacity by 20% to keep the energy unavailability indicator at the same level.

The analysis of the AED indicator in relation to S2P identifies the presence of a saturation bend, where increases in S2P do not significantly reduce the AED indicator. Therefore, the saturation bend together with the 5% limit on AED delimits a region in which to select the storage size, avoiding unnecessary oversizing.

It has also been observed that it is beneficial to oversize the BESS slightly. This not only prolongs its lifetime but also compensates for the reduction in capacity, which keeps the AED indicator at a low level. Specifically, for an intermediate power setpoint, it is concluded that selecting an S2P value of 2.1 instead of 1.9 extends battery life by almost twice as long.

The proposed model is adaptable and can be applied to other power generation technologies. Since the implemented algorithm performs hourly operations in a vectorial manner, it would be feasible to include an additional column vector in addition to the current PV production. Therefore, as a future line of work, all the simulations proposed in this article could be carried out using a combination of power generation technologies. Wind generation could be a suitable option to combine with PV generation due to their different generation patterns. Wind tends to produce more energy at night and on cloudy days, while solar tends to produce more energy in the middle of the day and under clear skies.

Author Contributions: Conceptualization, J.A.T.-G. and Á.A.B.-R.; methodology, J.A.T.-G. and Á.A.B.-R.; software, J.A.T.-G.; validation, J.A.T.-G. and Á.A.B.-R.; formal analysis, J.A.T.-G. and Á.A.B.-R.; investigation, J.A.T.-G. and Á.A.B.-R.; resources, J.A.T.-G.; data curation, J.A.T.-G.; writing—original draft preparation, J.A.T.-G. and Á.A.B.-R.; writing—review and editing, Á.A.B.-R.; visualization, J.A.T.-G.; supervision, Á.A.B.-R.; project administration, Á.A.B.-R. All authors have read and agreed to the published version of the manuscript.

Funding: This research received no external funding.

Data Availability Statement: Data are contained within the article.

Conflicts of Interest: The authors declare no conflicts of interest. The funders had no role in the design of the study; in the collection, analyses, or interpretation of data; in the writing of the manuscript; or in the decision to publish the results.

Abbreviations

PV	Photovoltaic
DG	Distributed generation
BESS	Battery energy storage systems
MV/LV	Medium Voltage/Low Voltage
PV-CPG	Photovoltaic Constant Power Generation
PCC	Point of common coupling
CF	Capacity factor
CPO _F	Constant Power Operation Factor
AED	Annual Energy Deviation
SoC	State of charge
SEI	Solid electrolyte interface
DoD	Depth of discharge
NEC	Number of equivalent cycles

References

1. World Energy Outlook 2023—Analysis. Available online: <https://www.iea.org/reports/world-energy-outlook-2023> (accessed on 1 February 2024).
2. Net Zero by 2050—Analysis. Available online: <https://www.iea.org/reports/net-zero-by-2050> (accessed on 8 February 2024).
3. Communication from the commission to the European parliament, the council, the European economic and social committee and the committee of the regions. A Blueprint to Safeguard Europe’s Water Resources. Available online: <https://www.eea.europa.eu/policy-documents/a-blueprint-to-safeguard-europes> (accessed on 1 February 2024).

4. Bayod-Rújula, A.A. Future Development of the Electricity Systems with Distributed Generation. *Energy* **2009**, *34*, 377–383. [CrossRef]
5. Xia, Q.; Debnath, S.; Saedifard, M.; Marthi, P.R.V.; Arifujaman, M. Energy Storage Sizing and Operation of an Integrated Utility-Scale PV+ESS Power Plant. In Proceedings of the 2020 IEEE Power & Energy Society Innovative Smart Grid Technologies Conference (ISGT), Washington, DC, USA, 17–20 February 2020; pp. 1–5.
6. U.S. Energy Information Administration. Form EIA-923, Power Plant Operations Report. Capacity Factors for Utility Scale 1215 Generators Primarily Using Non-Fossil Fuels. Available online: <https://www.iea.org/reports/grid-scale-storage> (accessed on 16 October 2023).
7. Bird, L.; Cochran, J.; Wang, X. *Wind and Solar Energy Curtailment: Experience and Practices in the United States*; Report No. NREL/TP-6A20-60983; National Renewable Energy Lab.(NREL): Golden, CO, USA, 2014; p. 1126842.
8. Abdelrazek, S.; Kamalasadani, S. A Weather-Based Optimal Storage Management Algorithm for PV Capacity Firming. *IEEE Trans. Ind. Appl.* **2016**, *52*, 5175–5184. [CrossRef]
9. Yoo, Y.; Jang, G.; Jung, S. A Study on Sizing of Substation for PV With Optimized Operation of BESS. *IEEE Access* **2020**, *8*, 214577–214585. [CrossRef]
10. Schmid, O.; Staffell, I. Experience Curve Data for Energy Storage Technologies. In *Monetizing Energy Storage—A Toolkit to Assess Future Cost and Value*; Oxford University Press: Oxford, UK, 2023.
11. Keerthisinghe, C.; Mickelson, E.; Kirschen, D.S.; Shih, N.; Gibson, S. Improved PV Forecasts for Capacity Firming. *IEEE Access* **2020**, *8*, 152173–152182. [CrossRef]
12. Ismael, S.; Abdel Aleem, S.; Abdelaziz, A.; Zobaa, A. State-of-the-Art of Hosting Capacity in Modern Power Systems with Distributed Generation. *Renew. Energy* **2019**, *130*, 1002–1020. [CrossRef]
13. Shin, H.; Hur, J. Optimal Energy Storage Sizing with Battery Augmentation for Renewable-Plus-Storage Power Plants. *IEEE Access* **2020**, *8*, 187730–187743. [CrossRef]
14. Shin, H.; Roh, J.H. Framework for Sizing of Energy Storage System Supplementing Photovoltaic Generation in Consideration of Battery Degradation. *IEEE Access* **2020**, *8*, 60246–60258. [CrossRef]
15. Rehman, W.; Bo, R.; Mehdipourpicha, H.; Kimball, J.W. Sizing battery energy storage and PV system in an extreme fast charging station considering uncertainties and battery degradation. *Appl. Energy* **2022**, *313*, 118745. [CrossRef]
16. Förstl, M.; Azuatalam, D.; Chapman, A.; Verbič, G.; Jossen, A.; Hesse, H. Assessment of residential battery storage systems and operation strategies considering battery aging. *Int. J. Energy Res.* **2019**, *44*, 718–731. [CrossRef]
17. Abdelrazek, S.; Kamalasadani, S. An Optimal Storage Management Algorithm for PV Capacity Firming Based on Weather Patterns. In Proceedings of the IEEE Industry Applications Society Annual Meeting, Addison, TX, USA, 18–22 October 2015; pp. 1–8.
18. Fujioka, H.; Yamamoto, H.; Okano, K. Effectiveness Verification of Energy Storage Systems toward Stable Electricity Supply with 100% Variable Renewable Energy. In Proceedings of the International Conference on Power and Energy Systems (ICPES), Colombo, Sri Lanka, 21–22 December 2018; pp. 60–64.
19. Roy, S.; Sinha, P.; Ismat Shah, S. Assessing the Techno-Economics and Environmental Attributes of Utility-Scale PV with Battery Energy Storage Systems (PVS) Compared to Conventional Gas Peakers for Providing Firm Capacity in California. *Energies* **2020**, *13*, 488. [CrossRef]
20. Doukas, D.I.; Papastergiou, K.; Bakas, P.; Marinopoulos, A. Energy Storage Sizing for Large Scale PV Power Plants Base-Load Operation—Comparative Study & Results. In Proceedings of the 2012 38th IEEE Photovoltaic Specialists Conference, Austin, TX, USA, 3–8 June 2012; pp. 000570–000574.
21. Tejero-Gómez, J.A.; Bayod-Rújula, Á.A. Analysis of Photovoltaic Plants with Battery Energy Storage Systems (PV-BESS) for Monthly Constant Power Operation. *Energies* **2023**, *16*, 4909. [CrossRef]
22. Bayod-Rújula, Á.A.; Tejero-Gómez, J.A. Analysis of the Hybridization of PV Plants with a BESS for Annual Constant Power Operation. *Energies* **2022**, *15*, 9063. [CrossRef]
23. Perez, R.; Taylor, M.; Hoff, T.; Ross, J.P. Reaching Consensus in the Definition of Photovoltaics Capacity Credit in the USA: A Practical Application of Satellite-Derived Solar Resource Data. *IEEE J. Sel. Top. Appl. Earth Obs. Remote Sens.* **2008**, *1*, 28–33. [CrossRef]
24. Photovoltaic Geographical Information System (PVGIS)—European Commission. Available online: https://joint-research-centre.ec.europa.eu/photovoltaic-geographical-information-system-pvgis_en (accessed on 3 January 2024).
25. Photovoltaic Module Datasheet. Model Tallmax TSM-DE15V(II) 490W Trinasolar. Available online: https://static.trinasolar.com/sites/default/files/DT-M-0007%20E%20Datasheet_TallmaxM_DE15V%28II%29_NA_EN_2022_1195A_web.pdf (accessed on 12 December 2023).
26. Photovoltaic Module Soiling Map. Available online: <https://www.nrel.gov/pv/soiling.html> (accessed on 12 December 2023).
27. Walker, A.; Desai, J. *Understanding Solar Photovoltaic System Performance: An Assessment of 75 Federal Photovoltaic Systems*; Report No. NREL/TP-5C00-80881; USDOE Office of Energy Efficiency and Renewable Energy (EERE): Washington, DC, USA, 2021; p. 1838130.
28. PV Inverter Datasheet. Model INGECON SUN 350TL M12 Ingeteam. Available online: https://www.ingetteam.com/es-es/sectores/energia-fotovoltaica/p15_24_727/330-350tl-m12.aspx (accessed on 16 January 2024).
29. Yang, H.; Zhang, Y.; Ma, Y.; Zhou, M.; Yang, X. Reliability Evaluation of Power Systems in the Presence of Energy Storage System as Demand Management Resource. *Int. J. Electr. Power Energy Syst.* **2019**, *110*, 1–10. [CrossRef]

30. Almazrouei, S.; Hamid, A.; Mehiri, A. Energy Management for Large-Scale Grid Connected PV—Batteries System. In Proceedings of the International Renewable and Sustainable Energy Conference (IRSEC), Tangier, Morocco, 4–7 December 2017; pp. 1–5.
31. Large-Scale Battery Energy Storage Inverter Datasheet. Model Ingecon Sun Storage 100TL Ingeteam. Available online: https://www.ingetteam.com/es-es/sectores/energia-fotovoltaica/p15_24_624_450/ingecon-sun-100tl.aspx (accessed on 10 January 2024).
32. Battery Energy Storage System Datasheet. Model TS-I HV 100 E TESVOLT. Available online: <https://www.tesvolt.com/en/products/e-serie/ts-i-hv-100-e.html> (accessed on 3 January 2024).
33. Masters, G. *Renewable and Efficient Electric Power Systems*; John Wiley & Sons, Ltd.: Hoboken, NJ, USA; Stanford University: Stanford, CA, USA, 2004; ISBN 978-0-471-66882-4.
34. IRENA. *Renewable Power Generation Costs in 2021*; International Renewable Energy Agency: Abu Dhabi, United Arab Emirates, 2022.
35. Fiorotti, R.; Fardin, J.F.; Encarnação, L.F.; Donadel, C.B. A Methodology to Determine the Firm Capacity of Distributed Generation Units. In Proceedings of the 2015 IEEE PES Innovative Smart Grid Technologies Latin America (ISGT LATAM), Montevideo, Uruguay, 5–7 October 2015; pp. 461–466.
36. Zhao, C.; Andersen, P.B.; Traholt, C.; Hashemi, S. Grid-Connected Battery Energy Storage System: A Review on Application and Integration. *Renew. Sustain. Energy Rev.* **2023**, *182*, 113400. [[CrossRef](#)]
37. Muenzel, V.; De Hoog, J.; Brazil, M.; Vishwanath, A.; Kalyanaraman, S. A Multi-Factor Battery Cycle Life Prediction Methodology for Optimal Battery Management. In Proceedings of the 2015 ACM Sixth International Conference on Future Energy Systems, Bangalore, India, 14–17 July 2015; ACM: New York, NY, USA; pp. 57–66.
38. Xu, B.; Zhao, J.; Zheng, T.; Litvinov, E.; Kirschen, D.S. Factoring the Cycle Aging Cost of Batteries Participating in Electricity Markets. In Proceedings of the 2018 IEEE Power & Energy Society General Meeting (PESGM), Portland, OR, USA, 5–10 August 2018. [[CrossRef](#)]
39. *ASTM E1049-85*; Standard Practices for Cycle Counting in Fatigue Analysis. ASTM International: West Conshohocken, PA, USA, 2017.
40. Hossain, M.A.; Pota, H.; Squartini, S.; Zaman, F.; Guerrero, J. Energy Scheduling of Community Microgrid with Battery Cost Using Particle Swarm Optimisation. *Appl. Energy* **2019**, *254*, 113723. [[CrossRef](#)]
41. Alhaider, F.; Klein, T.; Gerhard, S. A Simplified Methodology to Quickly Build a Degradation Prediction Model for Lithium-Ion Batteries. In Proceedings of the NEIS 2018 Conference on Sustainable Energy Supply and Energy Storage Systems, Hamburg, Germany, 20–21 September 2018; pp. 1–8.
42. Collath, N.; Tepe, B.; Englberger, S.; Jossen, A.; Hesse, H. Aging Aware Operation of Lithium-Ion Battery Energy Storage Systems: A Review. *J. Energy Storage* **2022**, *55*, 105634. [[CrossRef](#)]
43. Waldmann, T.; Wilka, M.; Kasper, M.; Fleischhammer, M.; Wohlfahrt-Mehrens, M. Temperature Dependent Ageing Mechanisms in Lithium-Ion Batteries—A Post-Mortem Study. *J. Power Sources* **2014**, *262*, 129–135. [[CrossRef](#)]
44. Gantenbein, S.; Schönleber, M.; Weiss, M.; Ivers-Tiffée, E. Capacity Fade in Lithium-Ion Batteries and Cyclic Aging over Various State-of-Charge Ranges. *Sustainability* **2019**, *11*, 6697. [[CrossRef](#)]
45. Fioriti, D.; Pellegrino, L.; Lutzemberger, G.; Micolano, E.; Poli, D. Optimal Sizing of Residential Battery Systems with Multi-Year Dynamics and a Novel Rainflow-Based Model of Storage Degradation: An Extensive Italian Case Study. *Electr. Power Syst. Res.* **2022**, *203*, 107675. [[CrossRef](#)]
46. Vetter, J.; Novák, P.; Wagner, M.R.; Veit, C.; Möller, K.-C.; Besenhard, J.O.; Winter, M.; Wohlfahrt-Mehrens, M.; Vogler, C.; Hammouche, A. Ageing Mechanisms in Lithium-Ion Batteries. *J. Power Sources* **2005**, *147*, 269–281. [[CrossRef](#)]
47. Edge, J.; O’Kane, S.; Prosser, R.; Kirkaldy, N.; Patel, A.; Hales, A.; Ghosh, A.; Ai, W.; Chen, J.; Jiang, J.; et al. Lithium Ion Battery Degradation: What You Need to Know. *Phys. Chem. Chem. Phys.* **2021**, *23*, 8200–8221. [[CrossRef](#)] [[PubMed](#)]
48. Liu, K.; Ashwin, T.R.; Hu, X.; Lucu, M.; Widanage, W.D. An Evaluation Study of Different Modelling Techniques for Calendar Ageing Prediction of Lithium-Ion Batteries. *Renew. Sustain. Energy Rev.* **2020**, *131*, 110017. [[CrossRef](#)]
49. Sayem, M.A.; Hannan, M.A.; Hossain Lipu, M.S.; Mannan, M.; Ker, P.J.; Hossain, M.J. State of the art of lithium-ion battery material potentials: An analytical evaluations, issues and future research directions. *J. Clean. Prod.* **2023**, *394*, 136246.
50. Birkel, C. *Oxford Battery Degradation Dataset 1*; University of Oxford: Oxford, UK, 2017.
51. Datasheet Battery Lithium-Ion Battery 24V—50Ah—1.28kWh—PowerBrick+. LiFePO4 Battery. Available online: <https://www.powertechsystems.eu/home/products/24v-lithium-battery-pack-powerbrick/50ah-24v-lithium-ion-battery-pack-1-28kwh-powerbrick-lithium/> (accessed on 26 July 2023).
52. Naumann, M.; Schimpe, M.; Keil, P.; Hesse, H.; Jossen, A. Analysis and Modeling of Calendar Aging of a Commercial LiFePO4/Graphite Cell. *J. Energy Storage* **2018**, *17*, 153–169. [[CrossRef](#)]
53. Wildfeuer, L.; Karger, A.; Aygül, D.; Wassiliadis, N.; Jossen, A.; Lienkamp, M. Experimental Degradation Study of a Commercial Lithium-Ion Battery. *J. Power Sources* **2023**, *560*, 232498. [[CrossRef](#)]

Disclaimer/Publisher’s Note: The statements, opinions and data contained in all publications are solely those of the individual author(s) and contributor(s) and not of MDPI and/or the editor(s). MDPI and/or the editor(s) disclaim responsibility for any injury to people or property resulting from any ideas, methods, instructions or products referred to in the content.